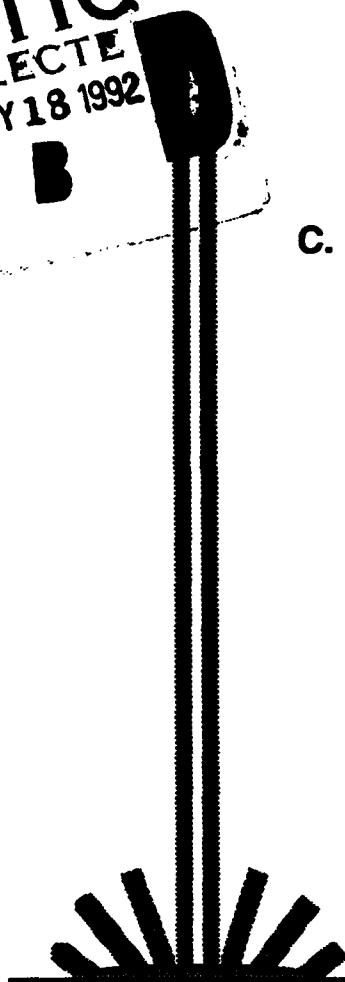AEOSR-TR· 92 0305

NON-EQUILIBRIUM SYNTHESIS BY LASER CLADDING OF Ni, Nb AND Mg ALLOYS FOR IMPROVED ENVIRONMENTAL RESISTANCE

J. Mazumder, Principal investigator
and
A. Kar, Faculty Associate
S. K. Tewari, Graduate Research Assistant
C. R. Ribaudo, Graduate Research Assistant(Graduated)

Laser Aided Materials Processing Laboratory
Department of Mechanical and Industrial Engineering
University of Illinois at Urbana-Champaign
1206 West Green Street
Urbana, Il 61801

92 5 15 40

REPORT DOCUMENTATION PAGE

Form Approved
OMB No. 0704-0188

Public reporting burden for this collection of information is estimated to average 1 hour per response, including the time for reviewing instructions, searching existing data sources, gathering and maintaining the data needed, and completing and reviewing the collection of information. Send comments regarding this burden estimate or any other aspect of this collection of information, including suggestions for reducing this burden, to Washington Headquarters Services, Directorate for Information Operations and Reports, 1215 Jefferson Davis Highway, Suite 1204, Arlington, VA 22202-4302, and to the Office of Management and Budget, Paperwork Reduction Project (0704-0188), Washington, DC 20503.

1. AGENCY USE ONLY (Leave blank)	2. REPORT DATE	3. REPORT TYPE AND DATES COVERED
	3-30-92	Final Report Nov. '88 – Oct. '91

4. TITLE AND SUBTITLE

Non-equilibrium Synthesis by Laser Cladding of Ni, Nb and Mg Alloys for Improved Environmental Resistance

5. FUNDING NUMBERS

AFOSR-89-0061

61102F
2304/A(

6. AUTHOR(S)

J. Mazumder, A. Kar, S. K. Tewari, and C. R. Ribaudo

7. PERFORMING ORGANIZATION NAME(S) AND ADDRESS(ES)

University of Illinois at Urbana-Champaign
Department of Mechanical & Industrial Engineering
1206 W. Green Street
Urbana, IL 61801

8. PERFORMING ORGANIZATION REPORT NUMBER

CLAMP-91A

9. SPONSORING/MONITORING AGENCY NAME(S) AND ADDRESS(ES)

Air Force Office of Scientific Research
Dr. Alan Rosenstein
Bolling Air Force Base
Washington, DC 20550

NC
AR

10. SPONSORING/MONITORING AGENCY REPORT NUMBER

AFOSR-89-0061

11. SUPPLEMENTARY NOTES

12a. DISTRIBUTION/AVAILABILITY STATEMENT

Approved for public release;
distribution unlimited.

12b. DISTRIBUTION CODE

13. ABSTRACT (Maximum 200 words)

The technique of laser surface modification provides a unique means of synthesizing novel nonequilibrium materials in near net shape. The goal of the proposed program is to develop a science base for synthesis of nonequilibrium metastable alloys by laser processing. This report summarizes experimental and theoretical studies carried out during the period of November 1988 to October 1991 on laser surface modification of Ni, Nb and Mg alloys for improved environmental resistance at high temperature. A microstructural evolution model of $NbAl_3$ was developed and the relative oxidation resistance of claddings of several Nb-based alloys were investigated. Initial work with V revealed that V increases the ductility, and decreases the oxidation resistance of laser clad $NbAl_3$. Oxidation behavior of alloys with Ti, B and Hf as a ternary alloy addition were identified. Oxidation tests at 800, 1200, and 1400°C were conducted on $NbAl_3$-0 at %B (0 B), $NbAl_3$-0.5 at %B (0.5 B), $NbAl_3$-1.0 at %B (1.0 B), $NbAl_3$-1.0 at B-3 at %Ti (3 Ti), $NbAl_3$-1.0 at %B-6 at %Ti (6 Ti) and $NbAl_3$-1.5 at %Hf (1.5 Hf) alloys. An external layer of α-alumina formed on samples of alloys 0.5 B and 1.0 B isothermally oxidized in air at 800, 1200 and 1400°C. A mixture of alumina and $NbAlO_4$ formed on the samples of alloy 0 B   exposed to same testing conditions. Alternating layers of alumina and (Continued on attached page.)

14. SUBJECT TERMS

15. NUMBER OF PAGES

89

16. PRICE CODE

17. SECURITY CLASSIFICATION OF REPORT	18. SECURITY CLASSIFICATION OF THIS PAGE	19. SECURITY CLASSIFICATION OF ABSTRACT	20. LIMITATION OF ABSTRACT
UNCLASSIFIED	UNCLASSIFIED	UNCLASSIFIED	

NSN 7540-01-280-5500

Standard Form 298 (Rev. 2-89)

NbAlO$_4$ were not observed in any of the samples as reported in literature for conventionally processed NbAl$_3$ oxidized under similar conditions. The parabolic rate constants for all the alloys, except 0 B, were comparable to that for isothermal oxidation of β-NiAl, at 1200 and 1400°C in 0.1 atm oxygen, which is a known alumina former. The main scientific findings are: the microstructure evolution during nonequilibrium synthesis of NbAl$_3$; identification of ternary alloying additions for improved oxidation resistance at 1400°C accompanied with improved ductility; and the identification of mechanism of protective oxide formation for Nb-alloys.

The objective of the work on Mg-based alloys was to improve the cladding process and to identify alloys with superior corrosion resistance. Three MgAl binary alloys and four MgAl ternary alloys containing Zr and Cr were clad. The use of a shielding chamber and alterations in the powder delivery system improved the bonding of the resulting clads. Relative amounts of phases in Mg$_{27}$Al$_{73}$ cladments were strongly affected by the specific energy input. Samples of Mg$_{27}$Al$_{73}$ exhibited resistance to 3.5% NaCl solution superior to that of cast Mg and AZ91B, a commercially produced alloy. The main scientific finding is laser clad alloy has superior corrosion resistance compared to commercial Mg alloys.

It was demonstrated that laser clad Ni$_{70}$M$_{20}$Cr$_7$Hf$_3$ (nominal) exhibited much superior oxidation resistance to commercial nickel superalloys such as Rene 80 at 1200°C. This increased operating temperature has long range ramifications on jet engine design with more favorable thrust/weight ratio. The main scientific finding is the new mechanism for improvement in alumina scale retention for laser clad Ni-Al-Cr-Hf alloys through micro-crack toughening.

The objective of the theoretical work was to develop a quantitative understanding of extended solid solubili$^{\prime}$ during nonequilibrium synthesis by laser. Nonequilibrium phase diagrams for Nb-Al, Ni-Al and Ni-Hf are developed based on this model. The most significant scientific achievement is the development of the model for nonequilibrium partition coefficient for concentrated binary alloy. This will improve the understanding of rapid solidification processes in general and nonequilibrium synthesis by laser in particular. This project has already led to significant advancement of the science for laser synthesis of nonequilibrium alloys.

Accession For		
NTIS GRA&I	☑	
DTIC TAB	☐	
Unannounced	☐	
Justification		
By		
Distribution/		
Availability Codes		
Dist	Avail and/or Special	
A-1		

FINAL REPORT

(November 1988 through October 1991)

NON-EQUILIBRIUM SYNTHESIS BY LASER CLADDING OF Ni, Nb AND Mg
ALLOYS FOR IMPROVED ENVIRONMENTAL RESISTANCE

Contract No. 89-0061

Submitted to
Air Force Office of Scientific Research
Building 410
Attn. Dr. A. Rosenstein
Bolling Air Force Base
Washington, DC 20332

J. Mazumder, Principal Investigator
and
A. Kar, Faculty Associate
S. K. Tewari, Graduate Research Assistant
C. R. Ribaudo, Graduate Research Assistant(Graduated)

Department of Mechanical and Industrial Engineering
University of Illinois at Urbana-Champaign
1206 West Green Street
Urbana, IL 61801

TABLE OF CONTENTS
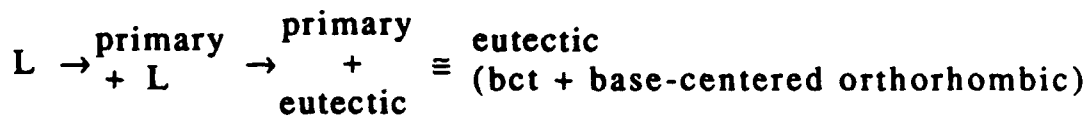
EXECUTIVE SUMMARY

The technique of laser surface modification provides a unique means of synthesizing novel nonequilibrium materials in near net shape. Environmental resistance of magnesium and niobium alloys can be improved by means of this laser based technique. A critical review of literature shows that magnesium and niobium alloys have potential aerospace applications for airframe and engine respectively, but their poor environmental resistance is the major hindrance to their application. The advantage of the laser surface modification technique is that since only the surface is being modified, enormous savings of alloying elements, which are often expensive or strategically important, can be achieved. Also, components with rapidly solidified structures can be made in near net shape by building multiple layers by laser cladding whereas the other Rapid Solidification Techniques (RST) require a consolidation process where temperature and pressure cycle induce phase transition in metastable phases.

The goal of the proposed program is to develop a science base for synthesis of nonequilibrium metastable alloys by laser processing. The specific objectives are: (1) to develop a fundamental understanding of the mechanism of formation of metastable phases involving extended solid solution and amorphous phase, (2) to study the effect of metastable crystalline and amorphous structure on (a) the high temperature oxidation properties of laser clad Nb alloys, and (b) the corrosion properties of laser clad Mg alloys, and (3) to develop the correlation between
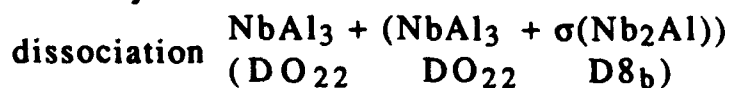
process parameters, microstructure and oxidation/corrosion properties of the above alloy.

This report summarizes experimental and theoretical studies carried out during the period of November 1988 to October 1991 on laser surface modification of Ni, Nb and Mg alloys for improved environmental resistance at high temperature. Major emphasis has been on the Nb-Al system. Microstructural evolution and oxidation properties of Ni and Nb alloys were examined. For Mg alloys, microstructural characterization and potentiodynamic corrosion testing were carried out. A one-dimensional diffusion model for the finite domain to examine the extended solid solubility in laser cladding developed under a previous (1985-1988) AFOSR program was applied to predict metastable phase diagram for Nb-Al alloy. Also, a model for nonequilibrium partition coefficient for concentrated solution was developed.

The objective of this Nb work was to use characterization results to develop a microstructural evolution model of $NbAl_3$ and to investigate the relative oxidation resistance of claddings of several Nb-based alloys. Using TEM (including CBED), STEM and SEM techniques, the probable phase evolution for $NbAl_3$ is determined as

$$L \rightarrow \begin{matrix} \text{primary} \\ + L \end{matrix} \rightarrow \begin{matrix} \text{primary} \\ + \\ \text{eutectic} \end{matrix} \cong \begin{matrix} \text{eutectic} \\ \text{(bct + base-centered orthorhombic)} \end{matrix}$$

$$\begin{matrix} \text{Primary} \\ \text{dissociation} \end{matrix} \quad \begin{matrix} NbAl_3 + (NbAl_3 + \sigma(Nb_2Al)) \\ (DO_{22} \quad\quad DO_{22} \quad\quad D8_b) \end{matrix}$$

Subsequently, the effect of the addition of ternary alloying elements on the oxidation behavior and the ductility of laser clad NbAl$_3$ alloys were studied. Initial work with V revealed that V suppresses the primary phase, increases the ductility, and decreases the oxidation resistance of NbAl$_3$.

Oxidation behavior of alloys with Ti, B and Hf as a ternary alloy addition were identified from the isothermal oxidation test at 1200°C in 60 cc/min dry air. Based on the results, oxidation tests at 800 and 1400°C were also conducted on NbAl$_3$-0 at %B (0 B), NbAl$_3$-0.5 at %B (0.5 B), NbAl$_3$-1.0 at %B (1.0 B), NbAl$_3$-1.0 atB-3 at %Ti (3 Ti), NbAl$_3$-1.0 at %B-6 at %Ti (6 Ti) and NbAl$_3$-1.5 at %Hf (1.5 Hf) alloys. Differential Thermal Analysis (DTA) used to determine phase transformations occurring below 1500°C indicated an endothermic phase change at about 650°C for 0.5 B, 1.0 B and 1.5 Hf alloys during heating runs.

Bulk chemical analysis results using atomic absorption spectroscopy indicated that 1.0 B alloy contains excess and 0 B and 0.5 B alloys are depleted in Al compared to that in stoichiometric NbAl$_3$. X-Ray Diffraction (XRD) used in conjunction with Scanning Electron Microscope (SEM) and Energy Dispersive X-ray (EDX) spectrometer showed that an external layer of α-alumina formed on samples of alloys 0.5 B and 1.0 B isothermally oxidized in air at 800, 1200 and 1400°C. A mixture of alumina and NbAlO$_4$ formed on the samples of alloy 0 B was exposed to same testing conditions. Alternating layers of alumina and NbAlO$_4$ were not observed in any of the samples as reported in literature for conventionally processed NbAl$_3$ oxidized under similar conditions. A layer of Nb$_2$Al formed

below the alumina layer in samples of 0.5 B and 1.0 B alloys oxidized at 1200 and 1400°C. This Nb_2Al layer formed only in regions where Nb_2Al was presented in significant amount in the unoxidized sample.

Preliminary results of the Vickers Diamond Pyramid microhardness test indicated that alloys 1.0 B, 3 Ti and 1.5 Hf may have acceptable ductility. The parabolic rate constants for all the alloys, except 0 B, were comparable to that for isothermal oxidation of β-NiAl, at 1200 and 1400°C in 0.1 atm oxygen, which is a known alumina former. The main scientific findings are: the microstructure evolution during nonequilibrium synthesis of $NbAl_3$; identification of ternary alloying additions for improved oxidation resistance at 1400°C accompanied with improved ductility; and the identification *of mechanism of protective oxide formation for Nb-alloys.*

The objective of the work on Mg-based alloys was to improve the cladding process and to identify alloys with superior corrosion resistance. Three MgAl binary alloys and four MgAl ternary alloys containing Zr and Cr were clad. The use of a shielding chamber and alterations in the powder delivery system improved the bonding of the resulting clads. SEM and DTA work indicated that the relative amounts of phases in $Mg_{27}Al_{73}$ cladments were strongly affected by the specific energy input. Samples of $Mg_{27}Al_{73}$ exhibited resistance to 3.5% NaCl solution superior to that of cast Mg and AZ91B, a commercially produced alloy. The main scientific finding is laser clad alloy has superior corrosion resistance compared to commercial Mg alloys.

The objective of the work on the Ni-Al-Cr-Hf system was to determine the impact of the extension of solid solubility of reactive elements such as Hf on the Ni-Cr-Al system for improved high temperature resistance. It was demonstrated that $Ni_{70}M_{20}Cr_7Hf_3$ (nominal) exhibited much superior oxidation resistance to commercial nickel superalloys such as Rene 80 at 1200°C. This increased operating temperature has long range ramifications on jet engine design with more favorable thrust/weight ratio. The main scientific finding is the new mechanism for improvement in alumina scale retention for laser clad Ni-Al-Cr-Hf alloys through micro-crack toughening.

The objective of the theoretical work was to develop a quantitative understanding of extended solid solubility during nonequilibrium synthesis by laser. Nonequilibrium phase diagrams for Nb-Al, Ni-Al and Ni-Hf are developed based on this model. The most significant scientific achievement is the development of the model for nonequilibrium partition coefficient for concentrated binary alloy. This will improve the understanding of rapid solidification processes in general and nonequilibrium synthesis by laser in particular.

This project has already led to significant advancement of the science for laser synthesis of nonequilibrium alloys. This is reflected in the various publications derived out of this work and the patent applied for by AFOSR for Ni-Cr-Al-Hf alloys. A list of publications from this project is given in Appendix A.

1. OXIDATION BEHAVIOR OF LASER CLAD NbAl₃ BASE ALLOYS

1.1 ABSTRACT

Prime objective of this work is to determine the effect of alloy additions on the oxidation behavior and ductility of laser clad $NbAl_3$ and to understand the mechanism(s) involved. Coatings of several Nb-Al base alloys were prepared by laser cladding mechanically mixed powder compositions on pure niobium substrates using a CW CO_2 laser with 10kW maximum power output. Alloys with adequate oxidation resistance were identified from the isothermal oxidation test at 1200°C in 60cc/min dry air. Based on the results, oxidation tests at 800 and 1400°C were also conducted on $NbAl_3$-0at%B(0B), $NbAl_3$-0.5at%B(0.5B), $NbAl_3$-1.0at%B(1.0B), $NbAl_3$-1.0at%B-3at%Ti(3Ti), $NbAl_3$-1.0at%B-6at%Ti(6Ti) and $NbAl_3$-1.5at%Hf(1.5Hf) alloys. Differential Thermal Analysis (DTA) used to determine phase transformations occuring below 1500°C indicated an endothermic phase change at about 650°C for 0.5B, 1.0B and 1.5Hf alloys during heating runs. Bulk chemical analysis results using atomic absorption spectroscopy indicated that 1.0B alloy contains excess and 0B and 0.5B alloys are depleted in Al than that in stoichiometric $NbAl_3$. X-Ray Diffraction(XRD) used in conjunction with Scanning Electron Microscope(SEM) and Energy Dispersive X-Ray Spectrometer(EDX) showed that an external layer of α-alumina formed on samples of alloys 0.5B and 1.0B isothermally oxidized in air at 800, 1200 and 1400°C. A mixture of alumina and $NbAlO_4$ formed on the samples of alloy 0B exposed to same testing conditions. Alternating layers of alumina and $NbAlO_4$ were not observed in any of the samples as reported in literature for conventionally processed $NbAl_3$ oxidized under similar conditions. A layer of Nb_2Al formed below the alumina layer in samples of 0.5B and 1.0B alloys oxidized at 1200 and 1400°C. This Nb_2Al layer formed only in regions where Nb_2Al was present in significant amount in the unoxidized sample. Preliminary results of Vickers Diamond Pyramid microhardness test indicated that alloys

1.0B, 3Ti and 1.5Hf may have acceptable ductility. The parabolic rate constants for all the alloys, except 0B, were comparable to that for isothermal oxidation of β-NiAl, at 1200 and 1400°C in 0.1 atm. oxygen, which is a known alumina former.

1.2 INTRODUCTION

$NbAl_3$ because of its low density (4.5gm/cc) and high melting point (1680±5°C) is a prime candidate for high temperature structural applications. It also has the best oxidation properties among all the Nb-Al alloys(3). During isothermal oxidation in air at temperatures 1200°C and above a protective alumina layer forms on $NbAl_3$(3, 4, 5). However, growth of alumina is not sustained due to formation and subsequent rapid oxidation of Nb_2Al into $NbAlO_4$ beneath the initial oxide layer. Oxide consisting of alternate layers of Al_2O_3 and $NbAlO_4$ forms as a result(3, 4, 5). Wagner's(6) classical model for transition from internal to external oxidation of more reactive element in the alloy and 'gettering' effect(7) have been the basis of recent efforts to develop Nb-Al base alloys which oxidize with sustained growth of external alumina scale. Alloying additions of Ti, Cr, Si, V, Y and Zr in various combinations and amounts to $NbAl_3$ have resulted into alloys which form external scale of alumina during isothermal and cyclic oxidation in air at and above 1200°C(5, 8). $NbAl_3$ exposed to oxygen containing atmosphere at temperatures between 650 to 800°C crumbles into powder, probably, due to grain boundary disintegration known as 'pest phenomenon'. This can be prevented by adding about 1at% excess Al to $NbAl_3$(9, 10).

Like many other intermetallic compounds, $NbAl_3$ is brittle at room temperature due to insufficient number of deformation modes available in its DO_{22} crystal structure(11). Information about the ductility of oxidation resistant $NbAl_3$ base alloys developed so far has not been reported in literature. Poor room temperature ductility of $NbAl_3$ may be attributed to highly directional and heteropolar nature of interatomic bonds(12) due to sd(Nb)-p(Al) hybridization. Interstitial elements which act as donor of electrons may promote uniform distribution of electrons among various interatomic bonds. B,

C, O and N, in decreasing order of potency, act as donor of electrons to fill the d-band of transition metal(13). Therefore, addition of these elements may improve ductility by activating additional deformation modes in $NbAl_3$. DO_{22} structure is based on one of the simplest cubic ordered structures $L1_2$ which has the requisite five independent slip systems for homogeneous deformation. Many compounds with $L1_2$ structure are known to be considerably ductile. Recent efforts to stabilize $L1_2$ structure over $DO_{22}(14)$ in $NbAl_3$ by alloying according to the guidelines based on 'Phenomenological Structure Stability Maps'(15) have been unsuccessful. Although, $TiAl_3$, which also has DO_{22} structure, has been successfully stabilized into $L1_2$ by addition of Zn, Ni, Cu or Fe(16, 17, 18). The reasons for non-stabilization of $L1_2$ in $NbAl_3$ has been identified(19) as very large total energy difference between DO_{22} and $L1_2$ structures compared to that for $TiAl_3$.

In laser cladding process mechanically mixed powder(s) of desired alloy composition is delivered to the laser/substrate interaction point to form a melt pool which rapidly solidifies due to heat extraction by constantly moving substrate acting as a large heat sink(20, 21, 22). The clad so produced has very fine grain size and uniform distribution of phases. Extension of solid solubility may also be possible due to rapid heating and cooling rates inherent to the laser cladding process and good metallurgical bonding between clad and substrate is achieved(20, 21, 23, 24).

Addition of B and C may improve the ductility of $NbAl_3$ by acting as electron donors. Formation of external scale of alumina during oxidation of $NbAl_3$ may be promoted by addition of Ti, Cr and Si by 'gettering' effect because the standard Gibbs free energy for formation of their oxides is between that for the oxides of Al and Nb. Also Ti may increase the solubility-diffusivity product of Al and increase its activity in the alloy(5) and Hf being a highly reactive element may reduce the solubility-diffusivity product of O in the alloy(25). These factors promote formation of external scale of alumina. In the present study laser cladding process parameters have been established. Isothermal oxidation behavior of laser clad $NbAl_3$ alloys containing various amounts of B, Ti, Cr, Si, C and Hf is

examined in 60cc/min dry air at 800, 1200 and 1400°C. Nb rich Nb-Al alloys are also examined in order to identify possible ductile oxidation resistant alloys. The results obtained are compared with that from similar alloys produced by conventional processes.

1.3 EXPERIMENTAL PROCEDURE

The cladding apparatus consisted of powder delivery and laser beam optics systems. A 10kW AVCO HPL CW CO_2 laser operating in the TEM^*_{01} (ring shaped beam) mode was used. The experimental set-up is shown in figure-1. Commercially pure 6mm thick niobium plates were used as substrates. In order to increase the absorption of laser power substrates were sand blasted. Prior to cladding substrates were ultrasonically cleaned in methanol to remove the sand particles. A beam integrating optics was used for uniform intensity distribution to obtain even depth of penetration. This was accomplished with the help of a integrating mirror (f=625mm) made of molybdenum, which consisted of 36 10x10mm square mirrors focussing over a 12.5mm square area. Laser beam was subsequently redirected on the substrate with the help of a flat mirror and a spherical concave mirror (f=100mm). A rectangular beam of spot size 4x4.5mm was used at 6 to 8kW power. Laser power output was calibrated periodically during cladding. Powder was dispensed from an Accu-Rate^{TM} screw feeder and carried to the laser/substrate interaction point through a funnel and tube assembly by gravity and assist gas. Helium or a mixture of helium and argon was used as shielding and powder carrier gas. This set-up was used for cladding $NbAl_3$ with and without boron additions. Substrate was moved at a constant velocity of 50 to 75cm/min on a computer controlled translation stage and powder was delivered at a rate of 15 to 45gm/min.

A modified set-up was used for cladding all the remaining alloys. Laser beam was initially focussed on a plane mirror by F7 cassegrain optics. The beam was subsequently redirected on the substrate with the help of an oscillating flat mirror. Laser beam of 2mm diameter, produced with the help of flat mirrors, oscillating at
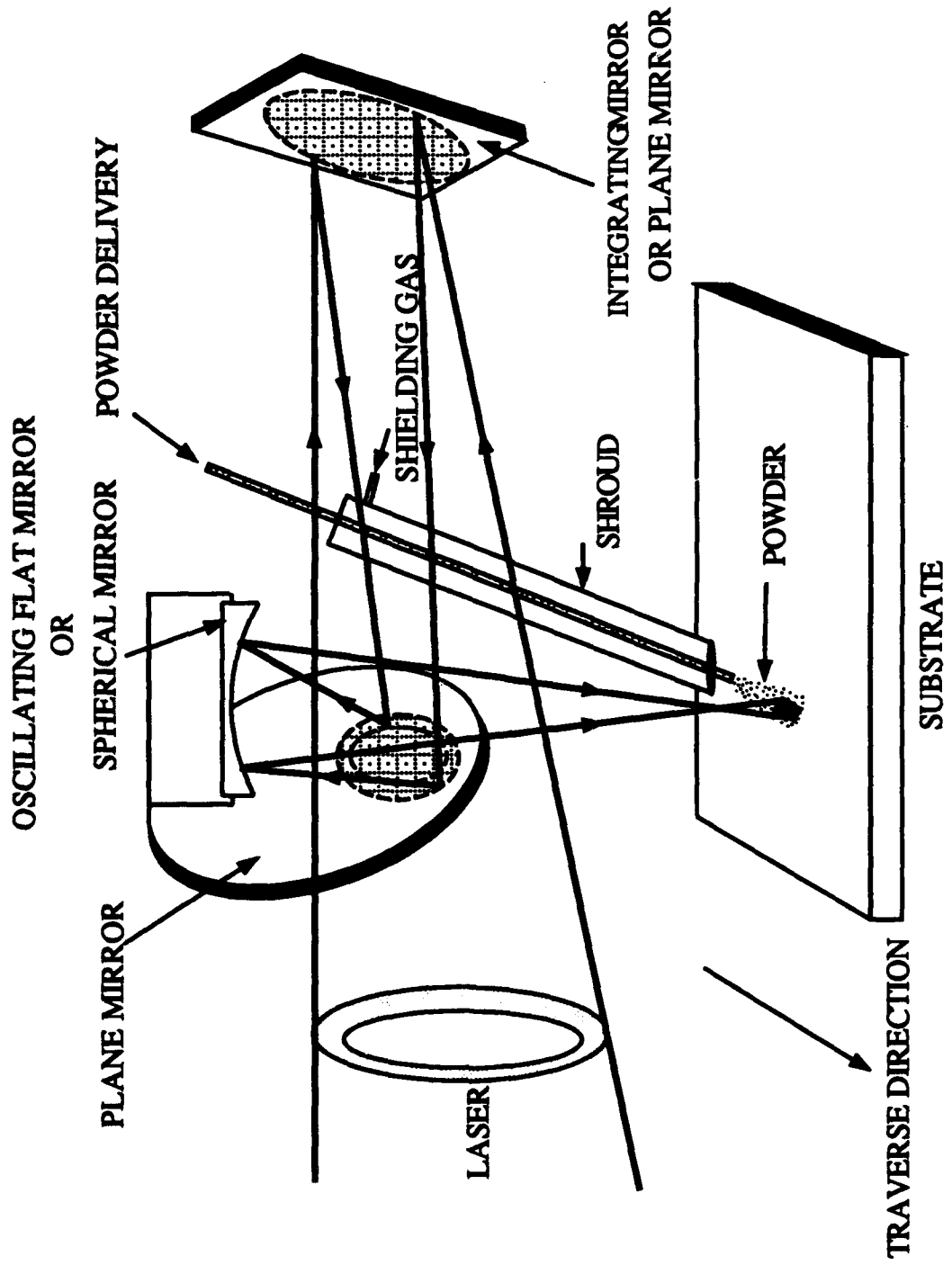
Figure-1 Schematic of experimental set-up for laser cladding.

100-110Hz with 2.5 to 3.5mm amplitude was used. This reduced the power requirements for producing acceptable clads by over 25%. A new powder dispenser was also designed which successfully eliminated nonuniformity of powder distribution. In this powder falls directly into the delivery tube from the container through spheroidal depressions in a rotating steel shaft rather than getting carried horizontally forward by a screw before falling into the tube. Feed rate can be controlled by changing the number or size of depressions on the shaft or its rotation speed. Very uniform clad were produced by using this set-up. Laser power of 4 to 6kW, powder feed rate of 15 to 30gm/min and substrate velocity of 30 to 51cm/min were used to produce these clads. In both the set-ups the final spot on the substrate was below focus to avoid keyhole and large depth of penetration. Pure powders were mechanically mixed and dried for 8 to 10 hours in protective argon atmosphere at 200°C. The powders used and their particle sizes are listed in Table-1.

Table-1 Powder Particle Size and Purity

Powder	Nb	Al	Ti	B	Hf	Cr	Si	C
Purity (wt%)	99.8	99	99.8	99	97.8	99.5	99	99.9
Size ($\leq\mu$m)	45	20&45-90	45	45	45	45	74	74

All compositions are in atomic percent in the entire text unless otherwise mentioned. Following powder compositions were cladded- $Nb_{25}Al_{75}$, $Nb_{25}Al_{74.5}B_{0.5}$, $Nb_{25}Al_{74}B_{1.0}$, $Nb_{22}Al_{74}Ti_3B_{1.0}$, $Nb_{19}Al_{74}Ti_6B_{1.0}$, $Nb_{24}Al_{74.5}Hf_{1.5}$, $Nb_{20}Al_{65}Cr_{15}$, $Nb_{25}Al_{60}Si_{15}$, $Nb_{25}Al_{74.8}C_{0.2}$, $Nb_{60}Al_{20}Cr_{20}$, $Nb_{60}Al_{20}Si_{20}$, $Nb_{45}Al_{40}Cr_{15}$, $Nb_{45}Al_{40}Si_{15}$, $Nb_{40}Al_{30}Cr_{20}Si_{10}$ and $Nb_{30}Al_{30}Cr_{20}Si_{10}Ti_{10}$. These compositions were selected based on the oxidation results reported in literature for similar alloys and factors described in the introduction section. Excess Al was added to compensate for loss due to evaporation during cladding. The amount was about 15 wt% in the first five alloys.The amount was reduced to about 2.5 wt% for rest of the compositions in which coarser Al powder was used.

Differential Thermal Analysis(DTA) of all the laser clad alloys was done using a Perkin Elmer DTA-1700 system capable of 1500°C maximum temperature. Heating and cooling runs were conducted at 20°C/min in 40cc/min flowing argon atmosphere.

Isothermal oxidation response of the clads was measured in 60cc/min flowing dry air for 8 or 20 hours using Perkin Elmer TGA-7 analyzer equipped with microbalance and continuous weight recording capability. The samples (approx. 1x2x5mm) from the clads were polished through 3μm alumina, ultrasonically cleaned and thoroughly rinsed successively in tri-chloroethane, acetone and methanol prior to loading into the cold furnace. After allowing sufficient time for experimental atmosphere to flush the unit the temperature was raised at a rate of 100°C/min to the desired value. Initially tests were conducted at 1200°C to identify alloys with good oxidation resistance and based upon the results tests at 800 and 1400°C were also done.

Microstructure and microchemistry of the clads were examined using a Hitachi S-800 Scanning Electron Microscope(SEM) equipped with Energy Dispersive X-Ray Spectrometer(EDX) with retractable Be-window. Morphology and cross sections of the oxidized samples were also examined using this microscope.

X-Ray Diffraction(XRD) studies of clads and oxidized samples were carried out using a Rigaku D-Max diffractometer with monochromatic Cu-Kα radiation source at 45kV and 20mA. Clads were examined in solid as well as powdered form. Samples were examined in varying $\theta/2\theta$ mode at a scan rate of 10°/min. Oxidized samples were mounted with the help of clay on a glass slide. This nondestructive method was used so that SEM/EDX investigation could be done on the same samples. Only for one sample of $NbAl_3+1at\%B$ alloy oxidized at 1400°C for 40 hours XRD was done on the oxide scrapped-off from the surface.

Microhardness measurements were carried out using a Vickers Diamond Pyramid microhardness tester. Several readings were taken along the length of the clad and representative indentations were photographically recorded.

A Cameca ims3f Secondary Ion Mass Spectrometer(SIMS) equipped with a resistive anode encoder imaging system was used to examine distribution of boron and oxygen in 0.5B and 1.0B alloys. Primary ion beam of Cs^+ at 17keV was used and secondary ions of B^- and O_2^- were analyzed from a $150\mu m^2$ circular image field. Primary beam diameter was $50\mu m$ and the lateral resolution of the instrument was of the order of $1\mu m$. Data were continuously recorded for sputtering time upto 10 minutes and the results obtained at the beginning and end were compared.

1.4 RESULTS

1.4.1 Thermogravimetric Analysis

Samples of alloys $NbAl_3$, $NbAl_3$-0.5B, $NbAl_3$-1.0B, $NbAl_3$-3Ti-1B, $NbAl_3$-6Ti-1B, $NbAl_3$-1.5Hf and $Nb_{20}Al_{65}Cr_{15}$ showed good oxidation resistance at 1200°C in air. Although other alloys showed parabolic oxidation behavior at 1200°C, the oxides spalled off followed by extremely rapid oxidation between 1200 to 650°C during cooling. Therefore no further work was done on these alloys. Weight gain per unit area(mg/cm^2) vs square root of oxidation time($min^{1/2}$) for the above alloys (except $Nb_{20}Al_{65}Cr_{15}$) at 800, 1200 and 1400°C is shown in figures-2, 3 and 4, respectively. Parabolic rate constants calculated(26) from these graphs after ascertaining linearity (fit for $R^2 \geq 0.97$) are listed in Table-2. Log k_p plotted against inverse of the absolute temperature of oxidation is shown in figure-5 for these alloys. Change in slope of this graph indicates change in the mechanism of oxidation.
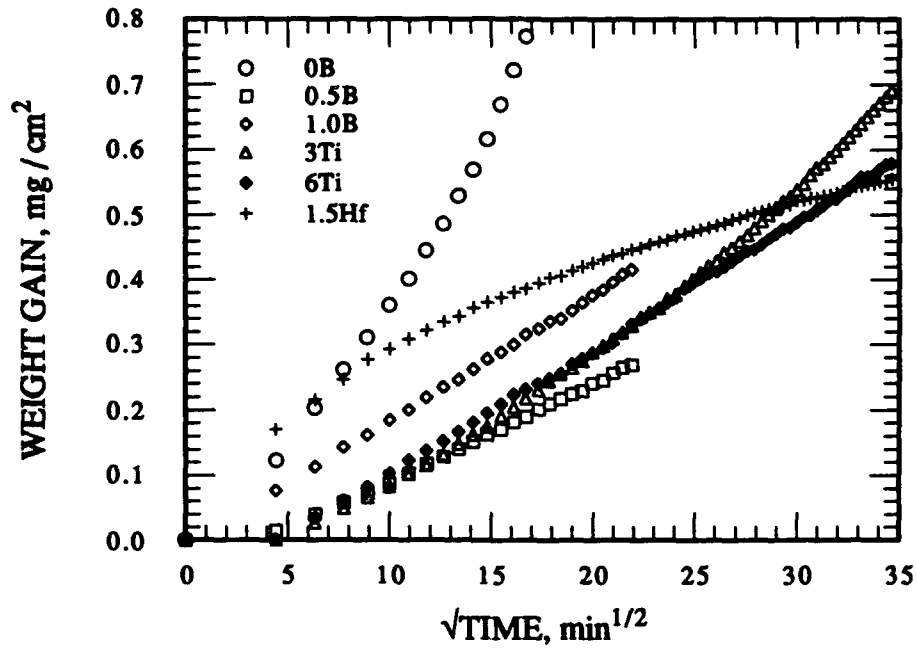
Figure-2 Isothermal oxidation at 800°C in air: weight gain per unit area as a function of square root of time for various alloys.
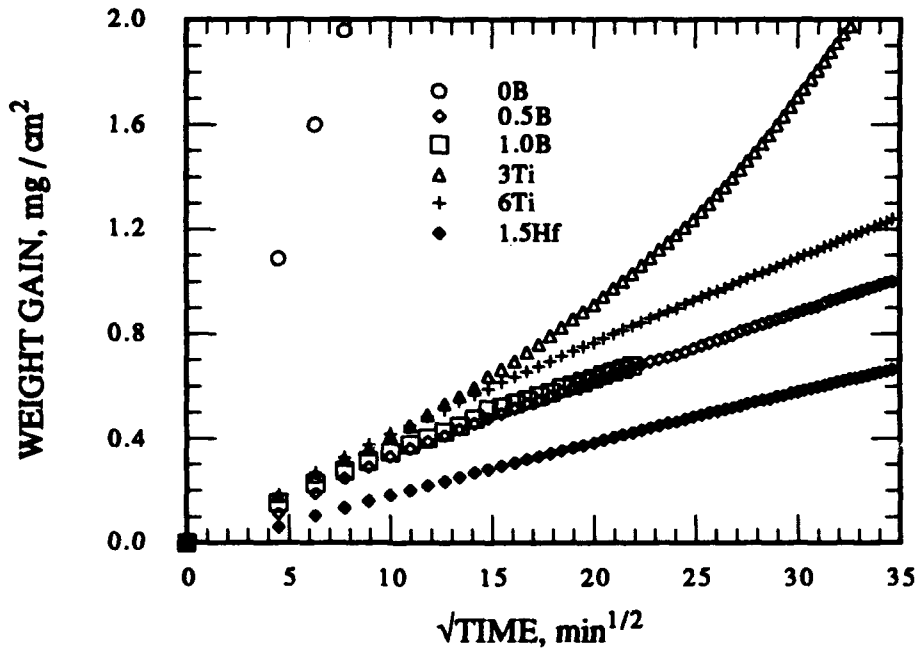

Figure-3 Isothermal oxidation at 1200°C in air: weight gain per unit area as a function of square root of time for various alloys.
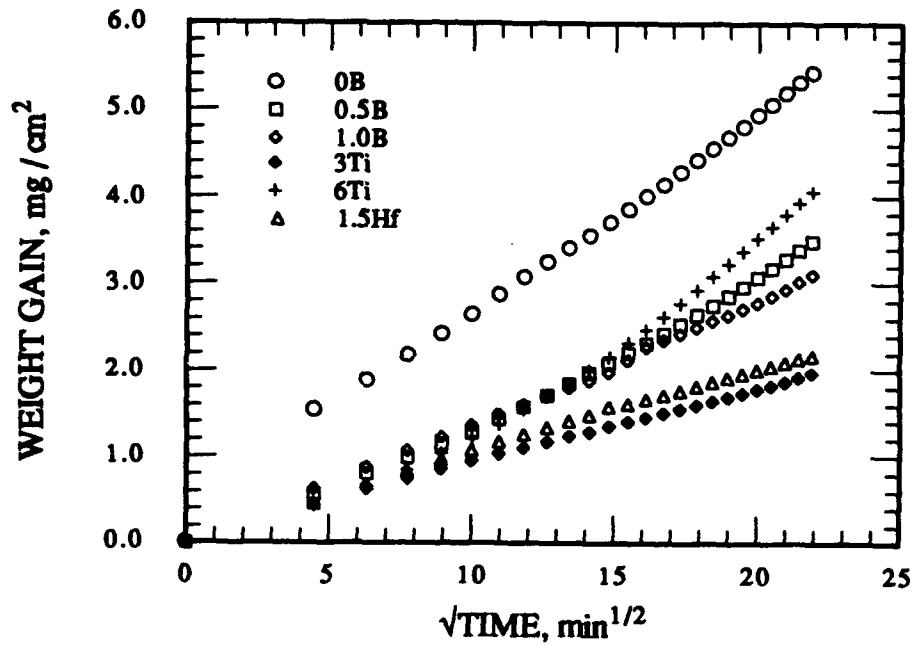
Figure-4 Isothermal oxidation at 1400°C in air: weight gain per unit area as a function of square root of time for various alloys.
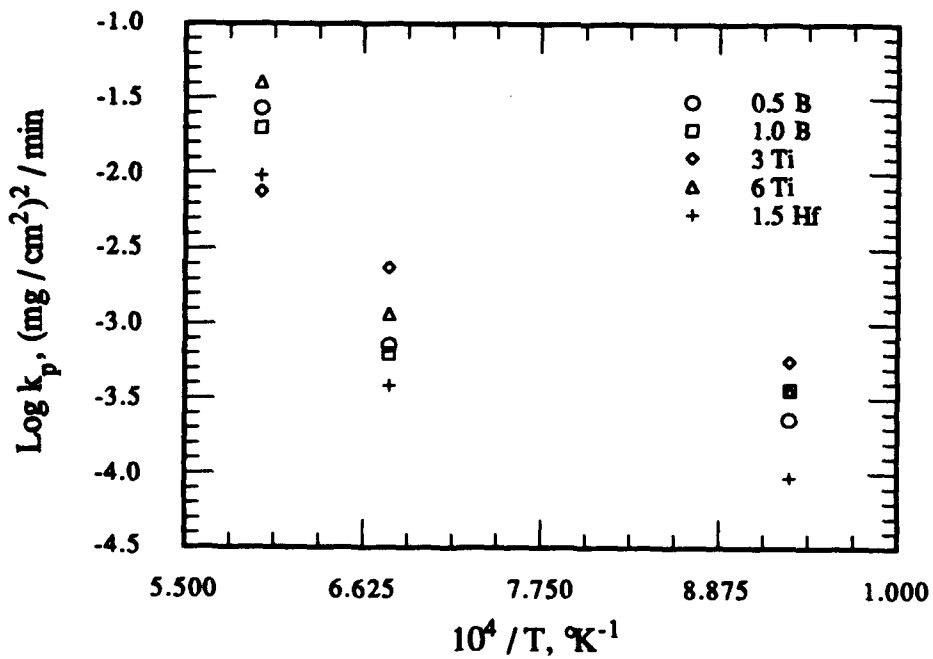

Figure-5 Arrhenius plot of rate constants for isothermal oxidation in air for various alloys.

Table-2 Value of Parabolic Rate Constant (x 10^{-4} $mg^2/cm^4.min$) for Isothermal Exposure to 60cc/min Air

Alloy	Referred in text as	Temperature (°C)		
		800	1200	1400
$NbAl_3$ (ref.3)	-	-	180	-
$NbAl_3$	0B	20.9, 87.7	652.3, 1556.3[#]	541
$NbAl_3$-0.5B	0.5B	2.31	7.2	268.8
$NbAl_3$-1.0B	1.0B	3.7	6.3	199.1
$NbAl_3$-3Ti-1B	3Ti	5.6	23.7, 94.6[#]	74.7
$NbAl_3$-6Ti-1B	6Ti	3.6	11.6	402.3
$NbAl_3$-1.5Hf	1.5Hf	0.9	3.85	95.4
$NiAl^*$ (ref. 27)	-	7.2×10^{-4}	2.68	44.69

[#] Sample cracked during the run.

[*] in 0.1 atm. oxygen; extrapolated data at 800° and 1400°C.

The results of isothermal oxidation test at 1200°C in air and DTA for the remaining alloys are summarized in Table-3. Qualitative observations of the oxides formed and ductility of the alloys are also reported.

Table-3   Results of DTA and Isothermal Oxidation at 1200°C in 60cc/min Air of other Laser Clad Alloys Examined in this Investigation.

Alloy	Ductility (qualitatively compared to NbAl$_3$)	DTA Transforma-tions at, °C	k_p, (mg/cm^2)^2/min.	Observations
Nb$_{60}$Al$_{20}$Cr$_{20}$	Very good	-	1.61(0-120 min.)	Sample intact, oxide greenish in color, spalled off during cooling (1100-900°C) followed by rapid oxidation.
Nb$_{60}$Al$_{20}$Si$_{20}$	Very good	-	0.97(0-120 min.)	Sample intact, oxide yellowish in color, spalled off during cooling (1000-625°C) followed by rapid oxidation. Oxide formed at 1400°C melted during the run.
Nb$_{20}$Al$_{65}$Cr$_{15}$	Poor	889, 1266, 1341, & 1488(M.P.)	1.38x10^{-3}	Sample intact, oxide dark gray in color, no spallation during cooling. At 800°C, sample intact, oxide dark black in color and k_p=4.87x10^{-5} (mg/cm^2)^2/min
Nb$_{25}$Al$_{60}$Si$_{15}$	Excellent	578, 602, 1203, & 1471(M.P.)	3.84x10^{-2}	Sample crumbled into yellowish gray powder and pieces, oxide spalled off during cooling (1050-625°C) followed by rapid oxidation.
Nb$_{22.5}$Al$_{75}$C$_{2.5}$	Good	660, 1195 &1250	1.72x10^{-2}	Sample crumbled into blackish gray powder, oxide spalled off during cooling (1100-500°C) followed by rapid oxidation.
Nb$_{25}$Al$_{74.8}$C$_{0.2}$	Poor	-	8.54x10^{-2}	Sample broken into pieces, oxide yellowish in color, oxide spalled off during cooling (1100-700°C) followed by rapid oxidation.
Nb$_{22}$Al$_{79.95}$Ti$_3$C$_{0.05}$	Good	-	2.47x10^{-3}	Sample intact, oxide grayish in color, no spallation.

Table-3......CONTD......

Alloy	Ductility (qualitatively compared to NbAl$_3$)	DTA Transformations at, °C	k_p, (mg/cm^2)^2/min.	Observations
Nb$_{23}$Al$_{71}$Cr$_2$Si$_2$Ti$_2$	Poor	-	5.01×10^{-4}	Sample intact, oxide blackish in color, no spallation.
Nb$_{23}$Al$_{69}$Cr$_2$Si$_2$Ti$_2$C	Poor	-	1.23×10^{-3}	Sample intact, oxide blackish in color, no spallation.
Nb$_{45}$Al$_{40}$Cr$_{15}$	Poor	-	0.38	Sample intact, oxide dark green in color, spalled off during cooling (1075-925°C) followed by rapid oxidation.
Nb$_{45}$Al$_{40}$Si$_{15}$	Good	-	3.84	Sample intact, oxide yellowish in color, oxide spalled off during cooling (1100-675°C) followed by rapid oxidation.
Nb$_{40}$Al$_{30}$Cr$_{20}$Si$_{10}$	Good	-	2.35×10^{-2}	Sample intact, oxide dark green in color, oxide spalled off during cooling (1125-1025°C) followed by rapid oxidation.
Nb$_{40}$Al$_{30}$Cr$_{20}$Si$_{10}$C	Good	-	1.54×10^{-2}	Sample intact, oxide dark green in color, oxide spalled off during cooling (1125-825°C) followed by rapid oxidation.
Nb$_{30}$Al$_{30}$Cr$_{20}$Si$_{10}$Ti$_{10}$	Good	-	9.49×10^{-3}	Sample intact, oxide dark green in color, oxide spalled off during cooling (1125-825°C) followed by rapid oxidation.

1.4.2 Differential Thermal Analysis

Endothermic phase change at about 650°C was observed for clad alloys 0.5B, 1.0B and 1.5Hf indicating presence of an Al rich phase. None of the alloys listed in Table-2 melted below 1500°C. $Nb_{20}Al_{65}Cr_{15}$ alloy showed best oxidation response at 800 and 1200°C. But this alloy melted at 1488°C and had phase transformations at 889, 1266 and 1341°C. Because of its low melting point further work was abandoned on this alloy. The DTA results are reported in Table-3.

1.4.3 Microstructure and Microchemistry

Results of the bulk chemical analysis obtained by atomic absorption spectroscopy (Galbraith Lab, TN) are given in Table-4 for 0B, 0.5B and 1.0B alloys.

Table-4 Bulk Chemical Analysis of the Alloys

Alloy	Composition (at%)	
	Aimed	Obtained
0B	Nb 75Al	Nb 70.02Al
0.5B	Nb 74.5Al 0.5B	Nb 73.35Al 0.34B
1.0B	Nb 74Al 1.0B	Nb 76.98Al 0.69B

Optical micrograph of a typical clad is shown in figure-6 (0.5B alloy). SEM micrographs of the clads of OB, 0.5B, 1.0B, 3Ti, 6Ti and 1.5Hf alloys are shown in figure-7(a) to (f), respectively. Results of the microchemistry of the phases present, obtained using SEM/EDX, are presented in Table-5.

1 mm

Figure-6 Optical micrograph of cross section of clad of 0.5B alloy.
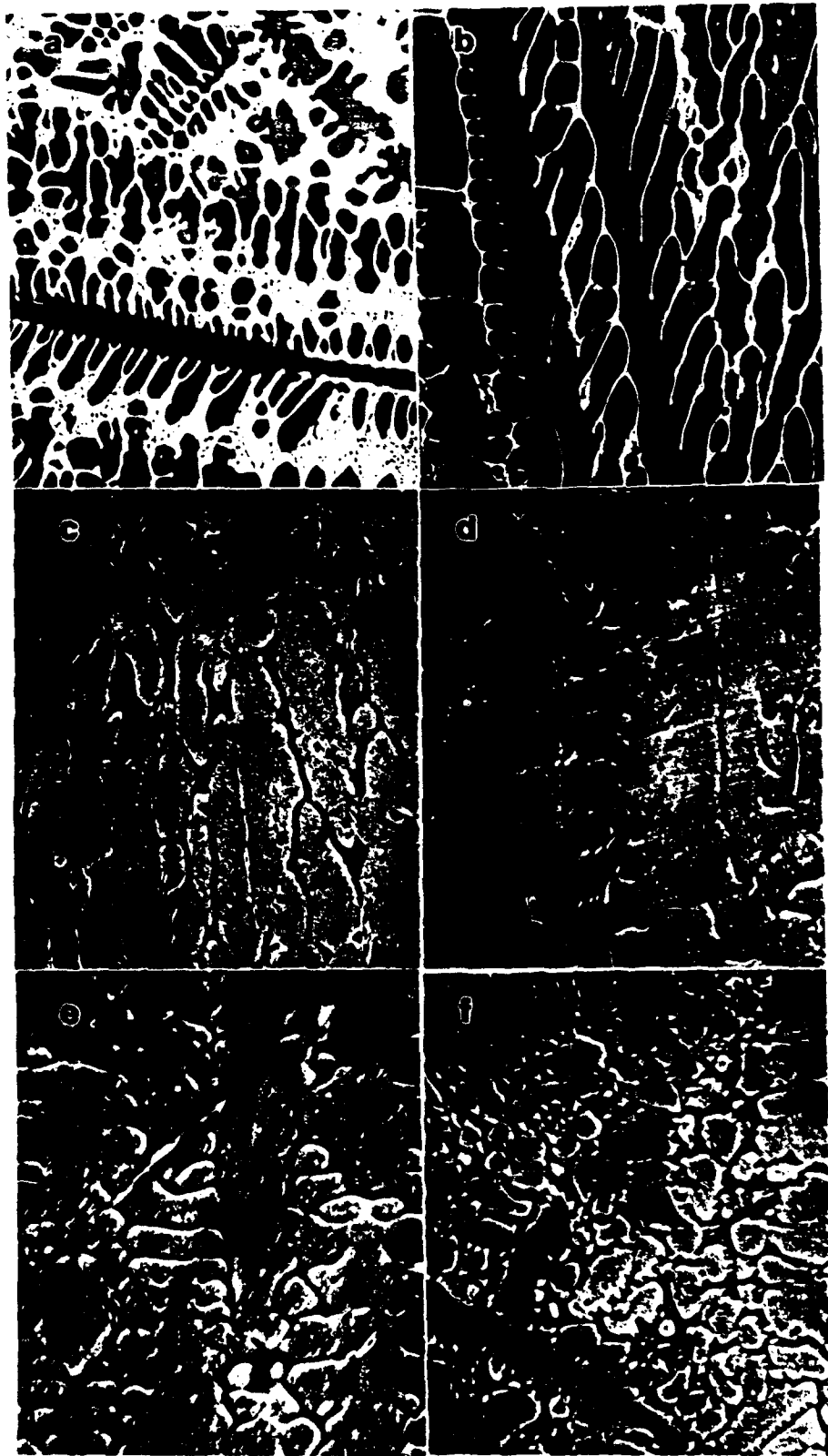
Figure-7 SEM micrographs of laser clad alloys (a) 0B, (b) 0.5B, (c) 1.0B,
(d) 3Ti, (e) 6Ti, and (f) 1.5Hf.

Table-5 Microchemical Analysis of the Alloys

Alloy	Phase/Feature	Composition(at%)			
		Nb	Al	Ti	Hf
0B, 0.5B & 1.0B	Large primary dendrite	27	73	-	-
	Bright interdendritic phase	57.4	42.6	-	-
0.5B & 1.0B	Dark interdendritic phase	10	90	-	-
3Ti	Large primary dendrites	25.9	72.7	1.4	-
	Dark interdendritic phase	14.3	71.5	14.2	-
	Long bright phase in the center of the clad	65.1	27.4	7.5	-
	Interdendritic bright phase near interface	33.5	56.5	10	-
6Ti	Large primary dendrites	26	72.6	1.4	-
	Dark interdendritic phase	3.7	80.7	15.6	-
	Long bright phase in the center of the clad	37.1	51.2	11.7	-
	Bright interdendritic phase near interface	38.5	48.8	12.7	-
1.5Hf	Large primary dendrites	26.3	73.1	-	0.6
	Dark interdendritic phase	6.4	91.4	-	2.2
	Dendrites near interface	25.3	73.4	-	1.3
	Bright phase near Interface	51	47.6	-	1.4
	Very bright small particles	34.3	20.1	-	45.6

1.4.4 X-Ray Diffraction

All XRD spectra were indexed by comparing with JCPDS diffraction data. Indexed XRD spectra of the powered samples of 0B, 0.5B and 1.0B alloys are shown in figures-8(a), (b) and (c), respectively. Main constituent of these alloys is $NbAl_3$. Nb_2Al is present in minor amount in 0.5B and 1.0B alloys and in significant amount in 0B alloy. XRD spectra from the solid as clad samples showed peaks at the same d-spacings, but their relative intensities substantially differed from that of the standard powder diffraction pattern. This suggests strongly preferred grain orientation. Indexed XRD spectra of the samples of 0B, 0.5B and 1.0B alloys oxidized at
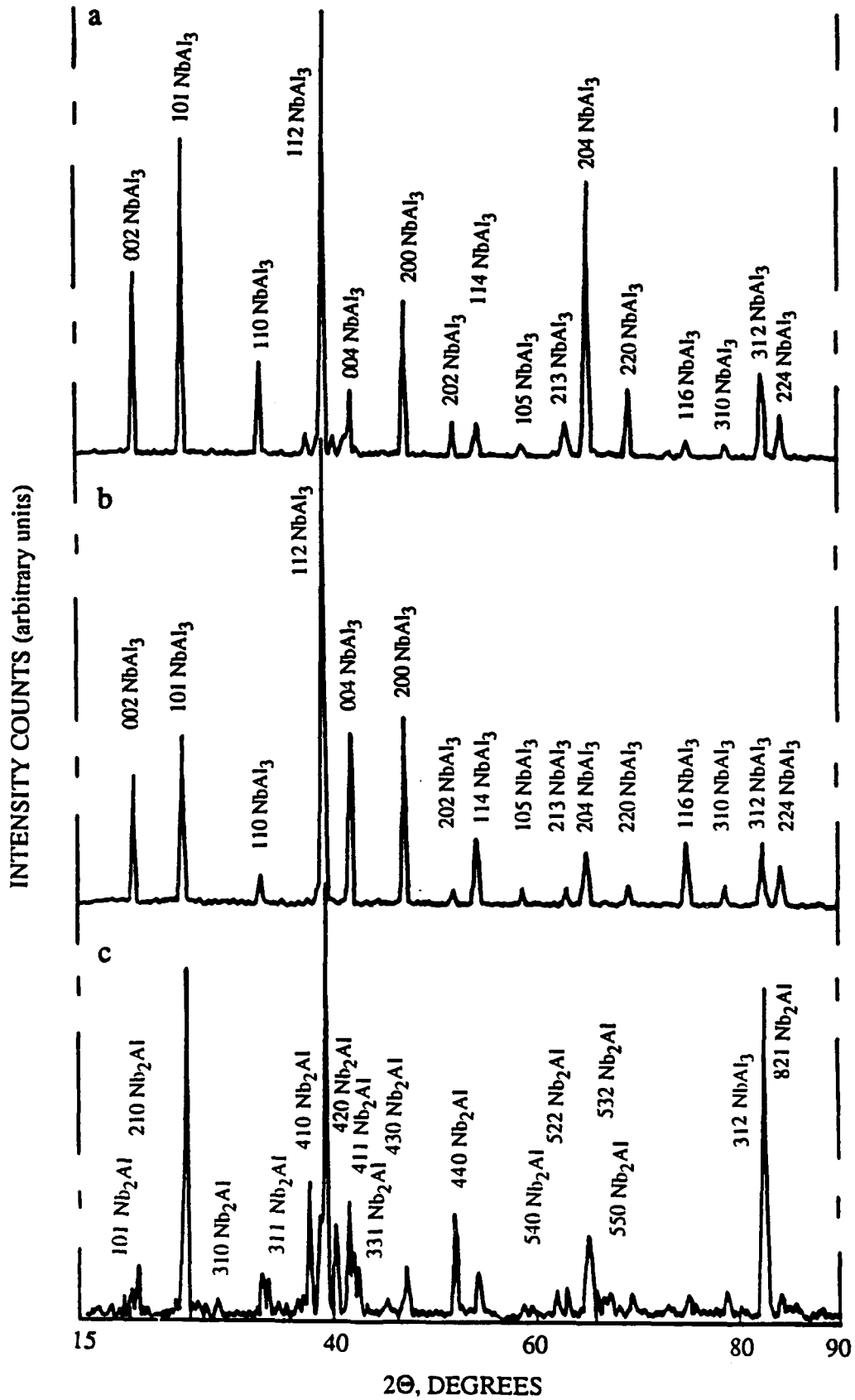
Figure-8 XRD spectra of laser clad alloys crushed into powder (a) 1.0B, (b) 0.5B, and (c) 0B.

800, 1200 and 1400°C are shown in figures-9, 10 and 11, respectively. Samples of 0B alloy oxidized at 1200 and 1400°C broke into pieces and no XRD was done on these samples. Oxide was scrapped off from a sample of 1.0B alloy oxidized at 1400°C in air for 40 hours and the spectra shown in figure-11(c) is from this oxide only. XRD results indicate that α-Al_2O_3 is the main constituent of the oxide formed on 0.5B and 1.0B alloys oxidized at 800, 1200 and 1400°C in air. $NbAlO_4$ is also present in very small amount. These two oxides are present in about equal proportions in the sample of 0B alloy oxidized at 800°C. Nb_2O_5, NbO and NbO_2 may also be present in trace amounts in the oxides formed but their presence can not be ascertained from XRD alone due to overlapping peaks.

1.4.5 Microexamination Of the Oxidized samples

SEM micrographs of the samples of 0B alloy oxidized at 800, 1200 and 1400°C are shown in figures-12(a), (b) and (c), respectively. Alloys 0.5B and 1.0B oxidized at 800, 1200 and 1400°C formed mostly alumina and had similar oxide morphology. Typical morphology of oxides formed at 800°C(1.0B), 1200°C(0.5B) and 1400°C(1.0B) is shown in SEM micrographs in figures-12(d), (e) and (f), respectively. SEM micrographs of the cross section of the sample of 0B alloy oxidized at 800°C are shown in figures-13(a) and (b). XRD and EDX results indicate that this dark oxide formed on the $NbAl_3$ dendrites consists of a mixture of alumina and $NbAlO_4$. The interdendritic Nb_2Al oxidized to pure $NbAlO_4$ which appears as white regions in oxide layer in the micrograph. EDX spectra from these two regions of the oxide layer are shown in figures-15(a) and (b), respectively. SEM micrographs of the cross section of 0.5B alloy oxidized at 800°C are shown in figures-13(c) and (d). Cross section of alloy 1.0B oxidized at 800°C is similar to that for 0.5B alloy and therefore not shown. A uniform layer of alumina formed on the samples. EDX spectra from the oxide layer is shown in figure-15(c). Aluminum rich phase near the surface oxidized internally forming alumina, however, it remained unoxidized at sites away from the interface. Cross sections of samples of the alloys 0.5B and 1.0B
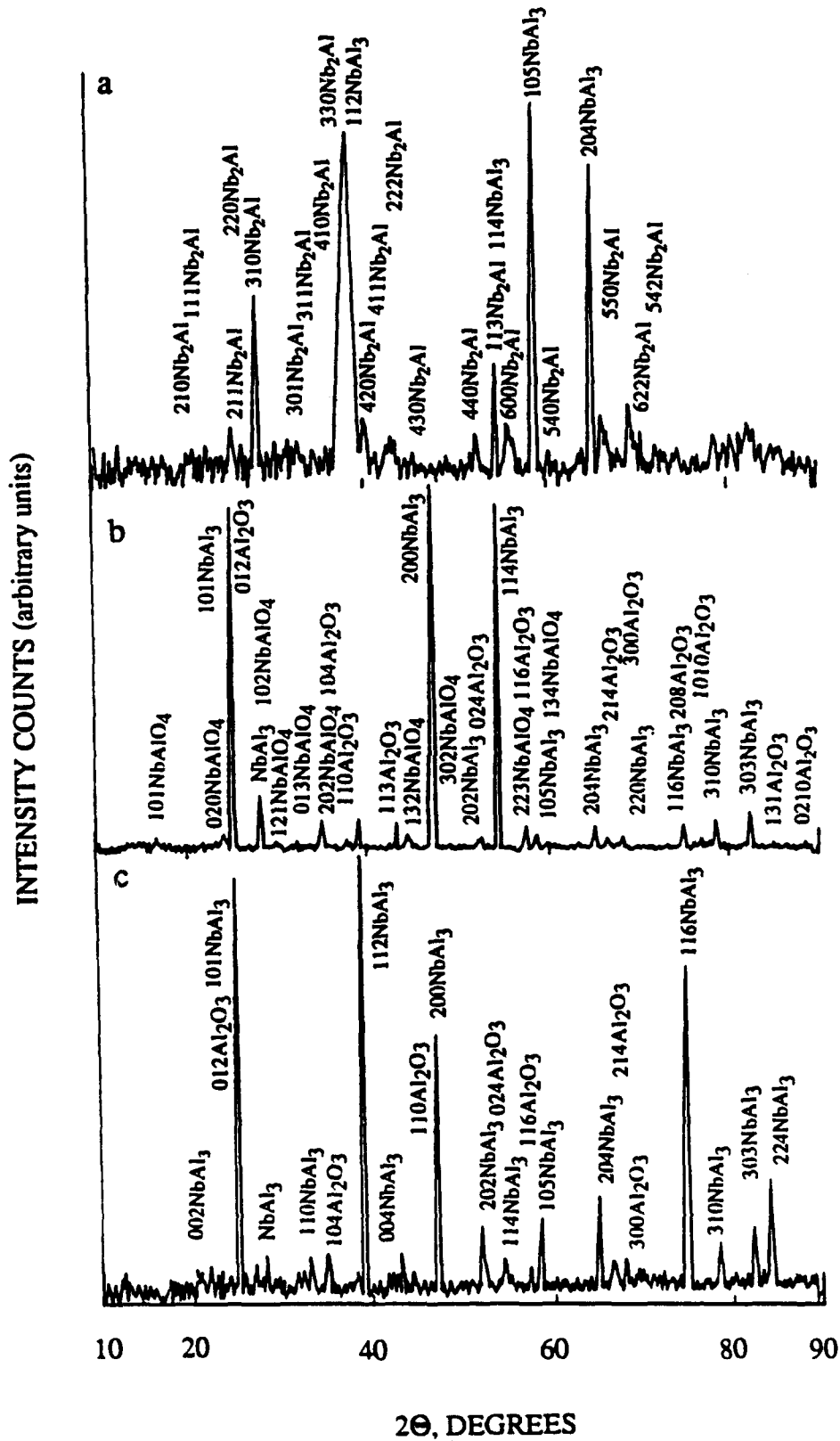
Figure-9 XRD spectra of alloys (a) 0B, (b) 0.5B, and (c) 1.0B after isothermal oxidation in air at 800°C.
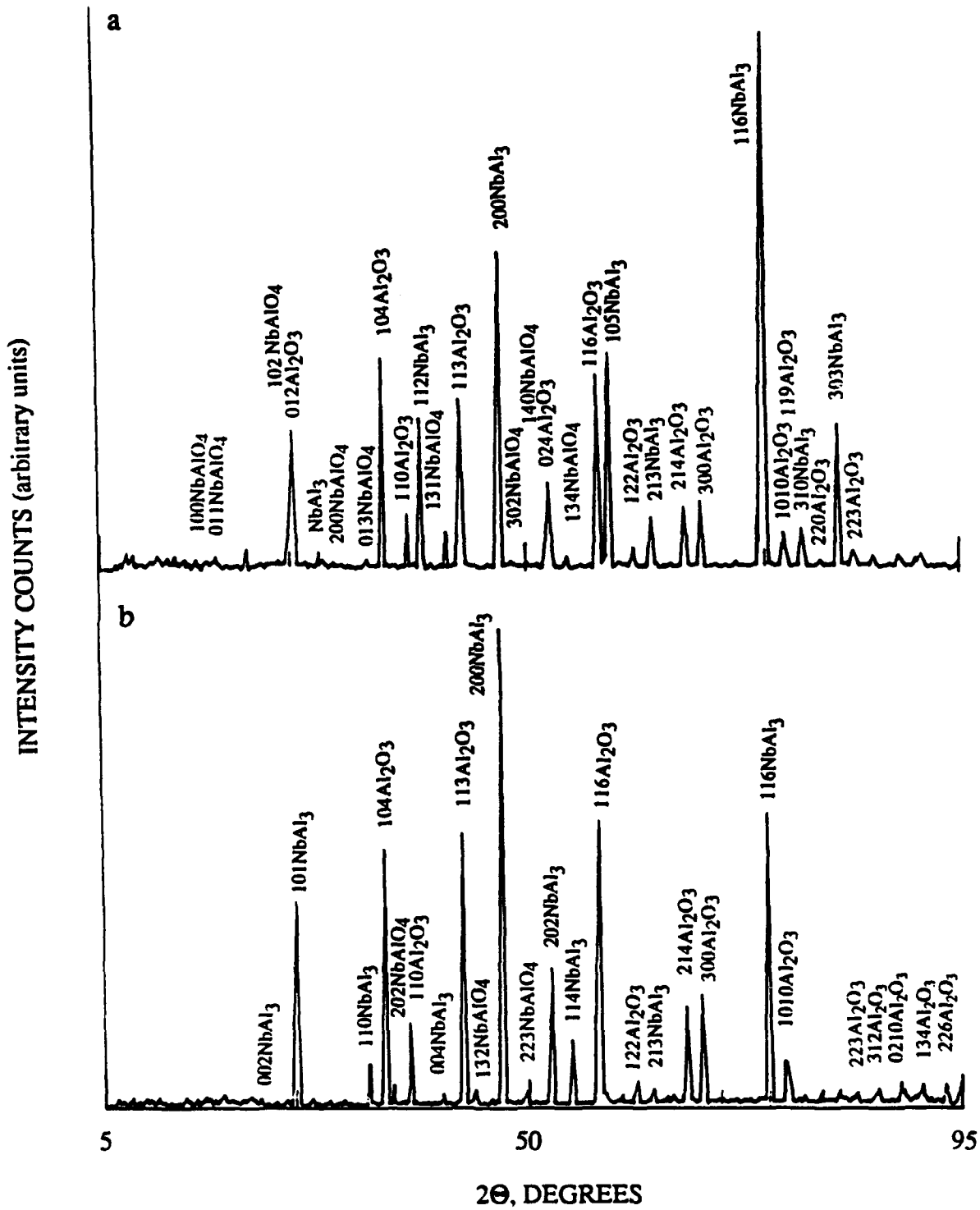
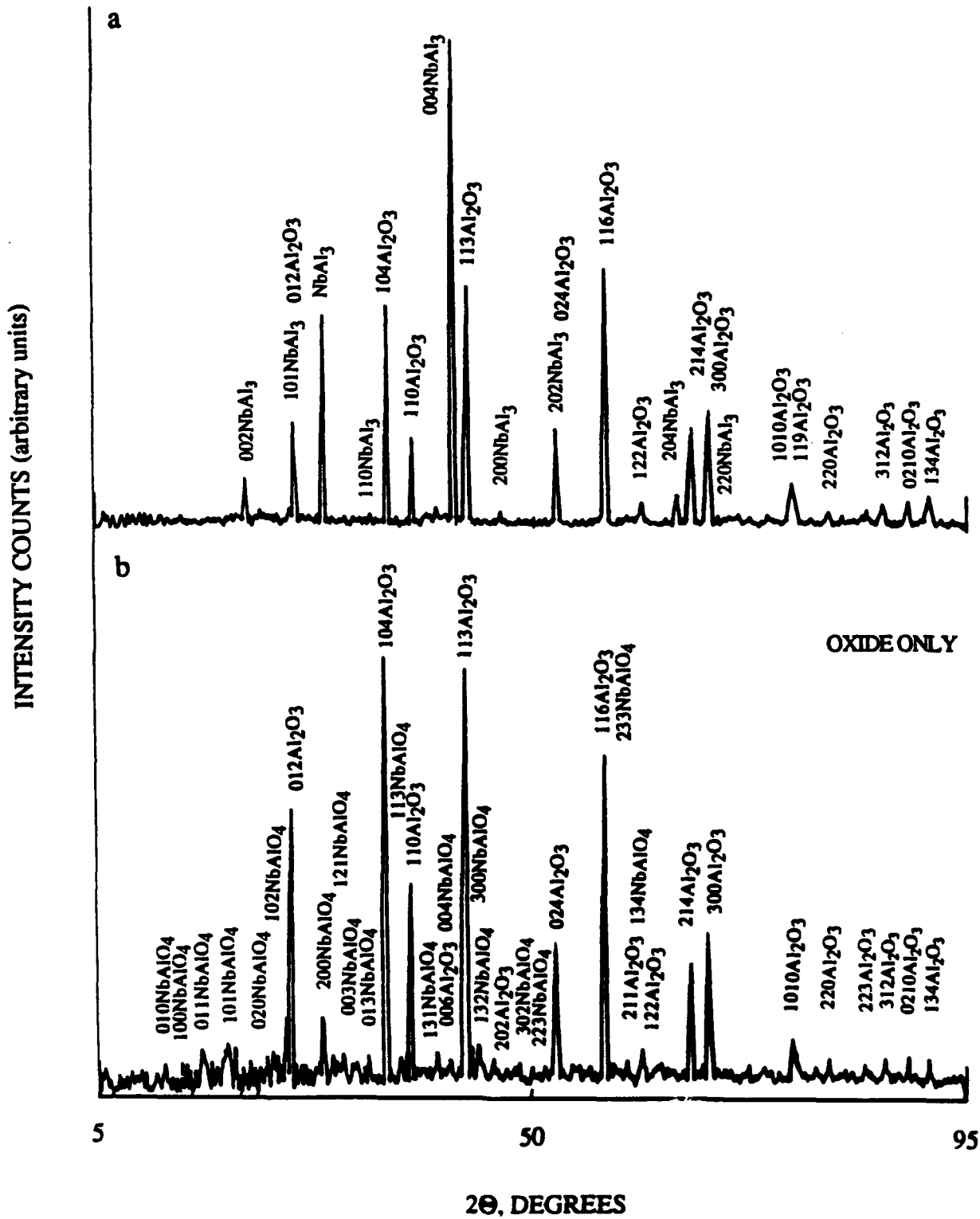Figure-10 XRD spectra of alloys (a) 0.5B, and (b) 1.0B after isothermal oxidation in air at 1200°C.

Figure-11   XRD spectra after isothermal oxidation in air at 1400°C of
(a) 0.5B alloy, and (b) of oxide scrapped-off from 1.0B alloy.

oxidized at 1200 and 1400°C are similar. SEM micrographs of cross section of 0.5B alloy oxidized at 1200°C are shown in figure-14(a) to (c). SEM micrographs of cross section of 1.0B alloy oxidized at 1400°C are shown in figure-14(d) and (e). External layer of alumina formed on the samples of 0.5B and 1.0B alloys oxidized at 1200 and 1400°C. A layer of Nb_2Al formed below the alumina layer only in regions where Nb_2Al is present as interdendritic phase in significant amount in the unoxidized sample. This can be observed in figures-14(b) and (c) for 0.5B alloy oxidized at 1200°C and in figure-14(e) for 1.0B alloy oxidized at 1400°C. No such layer formed below the alumina layer in regions where Nb_2Al is present in very small amount or not present at all as a second phase in the unoxidized sample as can be observed in the micrographs in figure-14(a) and (d) for 0.5B and 1.0B alloys oxidized at 1200°C and 1400°C, respectively. Nb_2Al wherever present as interdendritic second phase oxidized forming $NbAlO_4$. This $NbAlO_4$ appears as white oxide embedded in the alumina layer as seen clearly in the micrograph in figures-14(c). EDX spectra of these regions marked 1 & 2 in figure-14(c) are shown in figures-15(d) and (e), respectively.

1.4.6 Microhardness

Optical micrographs of the hardness indentations for the 0B, 0.5B, 1.0B, 3Ti, 6Ti and 1.5Hf alloys are shown in figure-16(a) to (f), respectively. The microhardness values measured are reported in Table-6.

Table-6 Microhardness(H_v) of the Alloys

Alloy	Microhardness(H_v), 500 gm load
0B	761
0.5B	622
1.0B	659
3Ti	634
6Ti	672
1.5Hf	261
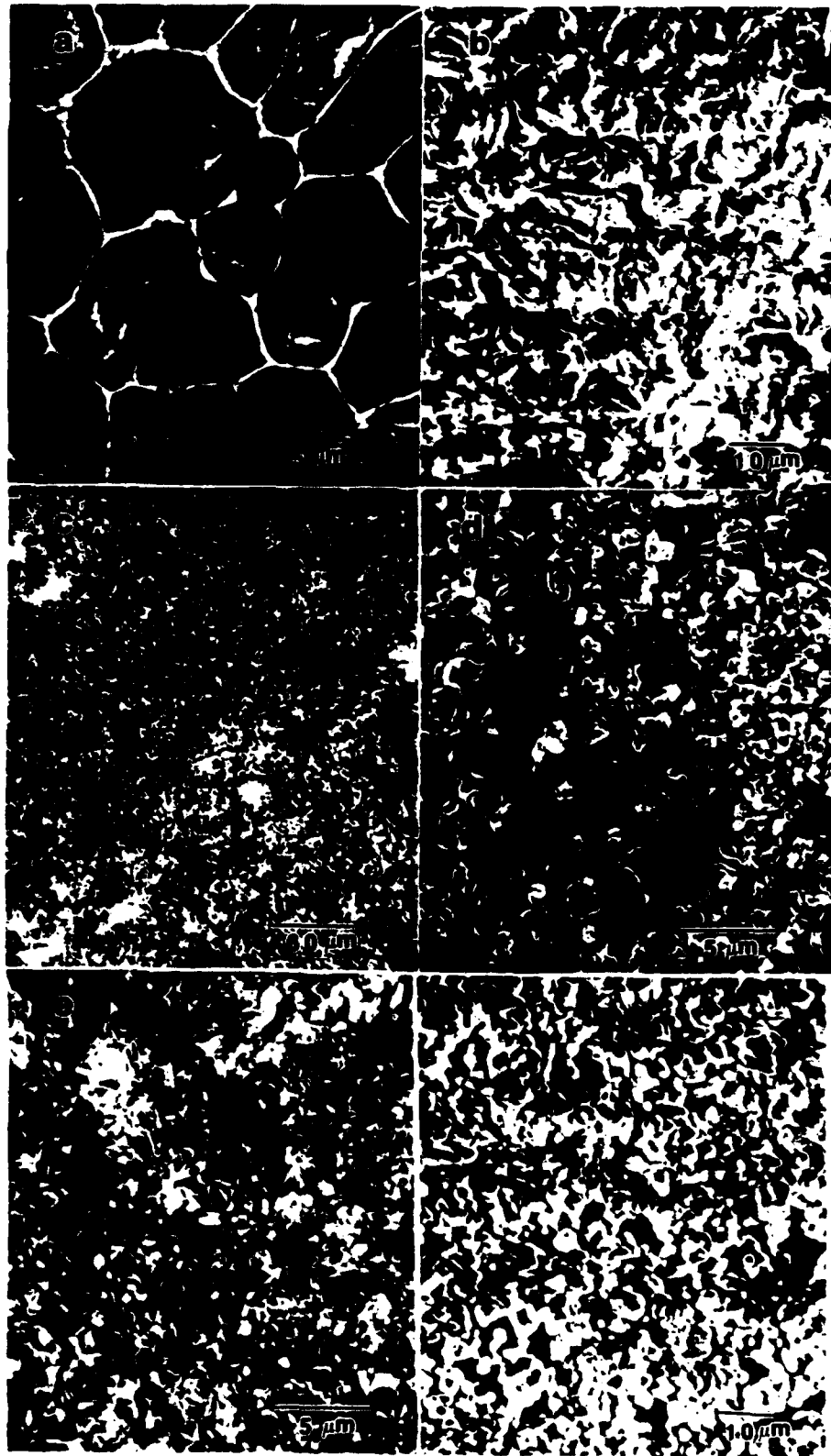
Figure-12 SEM micrographs of alloys after isothermal oxidation in air: 0B at (a) 800, (b) 1200, and (c) 1400°C; (d) 1.0B at 800°C; (e) 0.5B at 1200°C; and (f) 1.0B at 1400°C.
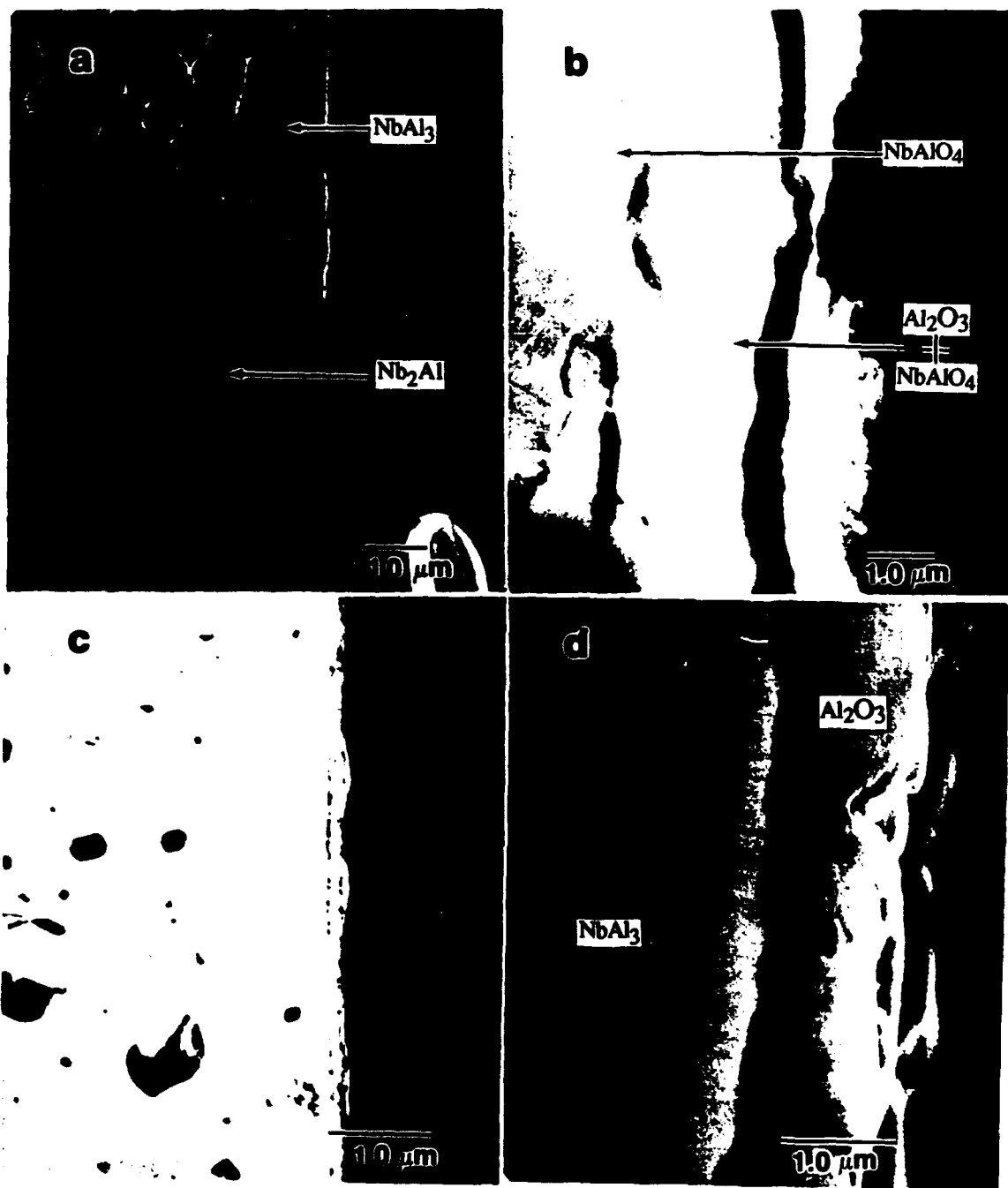
Figure-13   SEM micrographs of cross sections of samples oxidized in air at 800°C: (a) & (b) alloy 0B, and (c) & (d) alloy 0.5B.
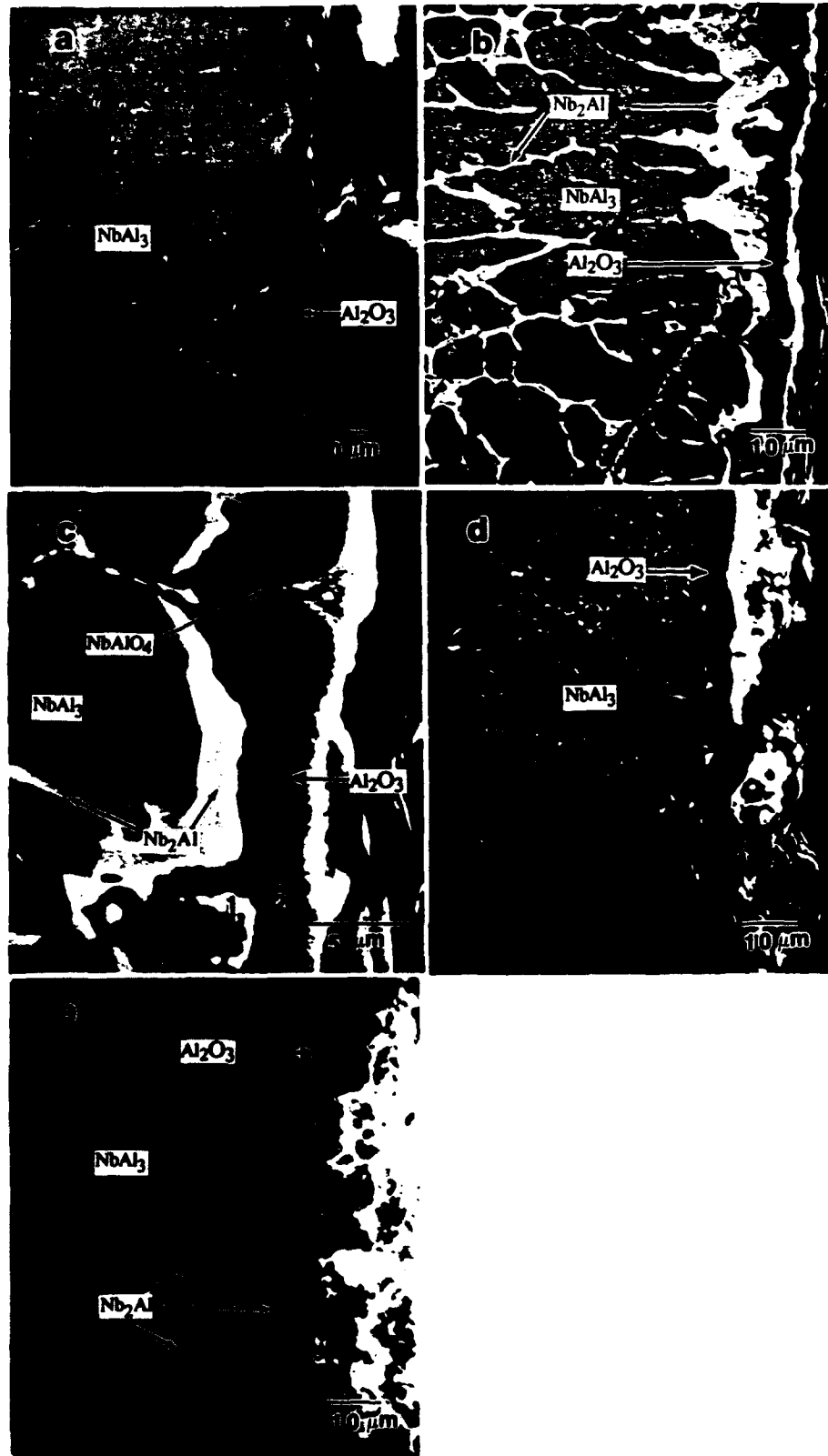
Figure-14 SEM micrographs of cross sections of samples oxidized in air: (a), (b) & (c) alloy 0.5B at 1200°C, and (d) & (e) alloy 1.0B at 1400°C.
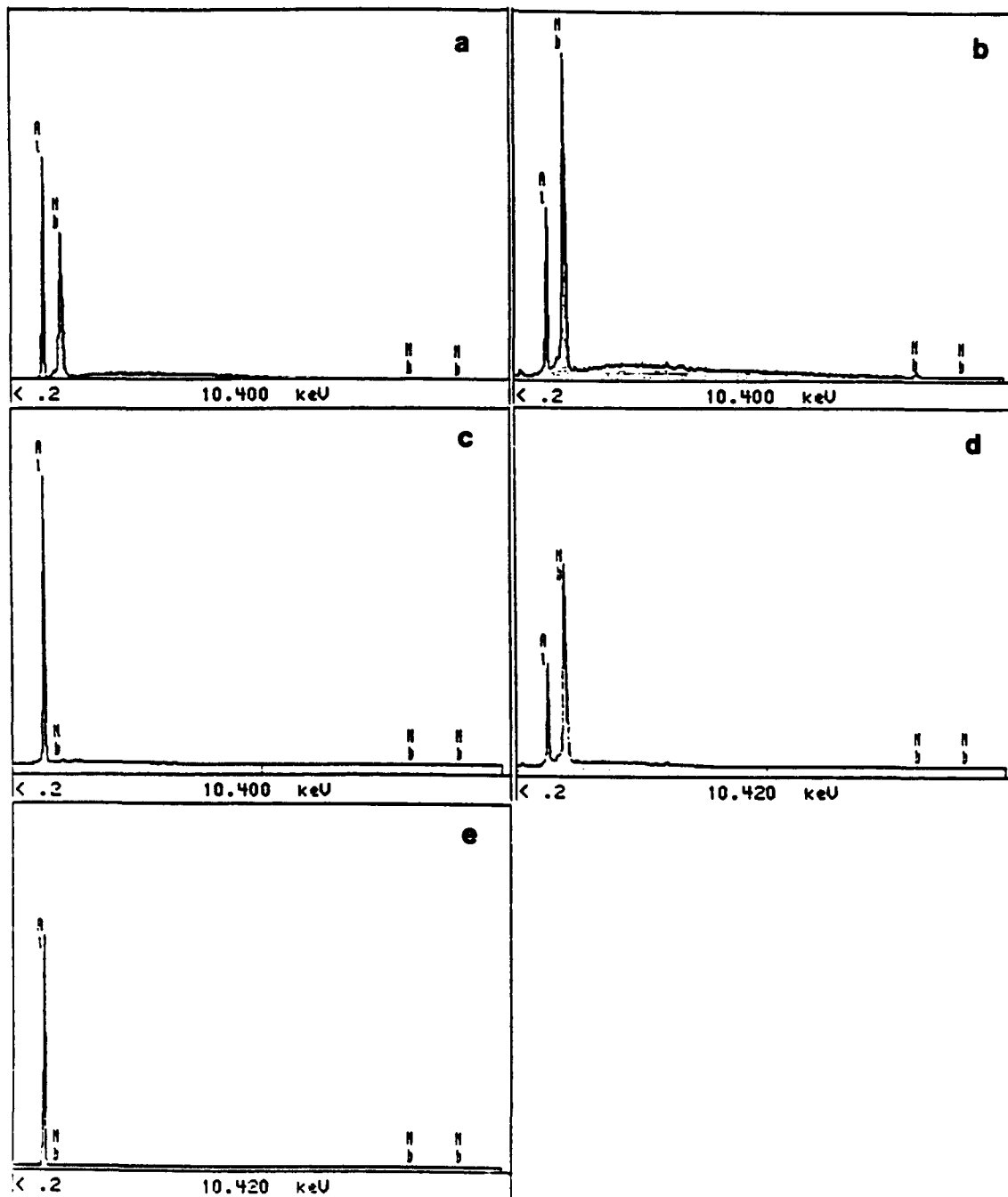
Figure-15 EDX spectra of (a) dark oxide and (b) bright oxide on 0B
alloy, and (c) granular oxide on 0.5B alloy after oxidation at
800°C in air(ref. Figures-12 and 13). EDX spectra (d) of
$NbAlO_4$ embedded in alumina(region 1 in Figure-14(c)), and
(e) of alumina(region 2 in Figure-14(c)) on 0.5B alloy after
isothermal oxidation at 1200°C in air.
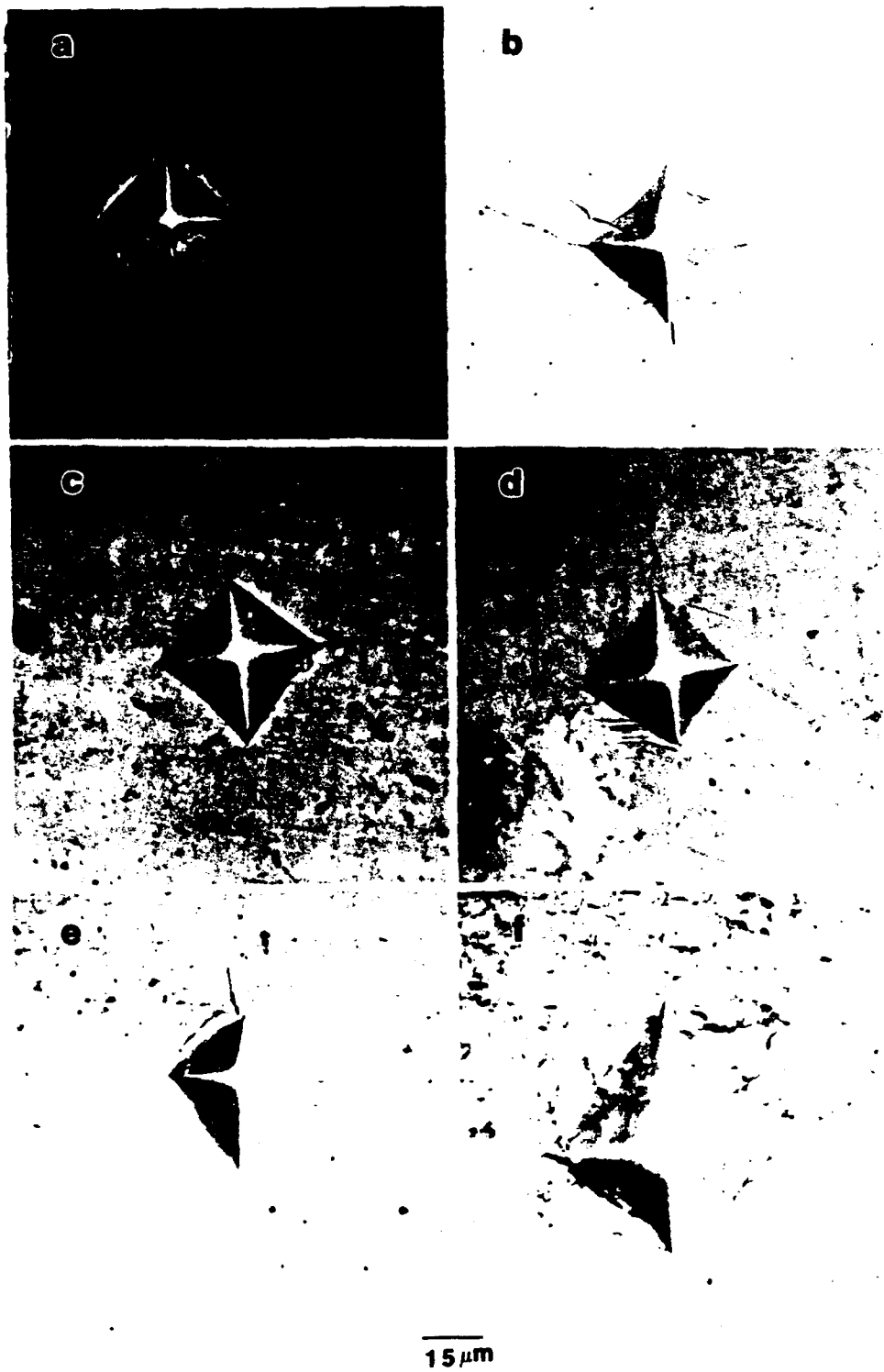
Figure-16 Microhardness indentations for laser clad alloys (a) 0B,
(b) 0.5B, (c) 1.0B, (d) 3Ti, (e) 6Ti, and (e) 1.5Hf.

For 1.5Hf alloy microhardness values taken along the length of a single clad varied from 783 to 261 H_v The value reported above is from region closest to place from where all samples for oxidation tests were taken. This much variation probably indicates composition variation. More investigation is needed to confirm this.

1.4.7 Secondary Ion Mass Spectroscopy(SIMS)

Preliminary results indicate that both boron and oxygen are not uniformly distributed in 0.5B and 1.0B alloys. SIMS images of B^- and O_2^- from these alloys were similar and did not vary with the sputtering time. Typical SIMS images of B^- and O_2^- from 1.0B alloy after 10 minutes of sputtering are shown in figures-17(a) and (b), respectively. Bright areas represent regions of concentration of these elements in the analyzed area. However, due to limited resolution of the instrument used and fine microstructure of these laser clad alloys, specific information about segregation could not be obtained.

1.5 DISCUSSION

Laser cladding parameters have been established. Parameters other than those used for cladding result into either too much penetration and dilution or insufficient bonding and defects at the clad/substrate interface. Uniformity of the clads has been improved significantly using the new powder dispenser. Power requirements for producing acceptable clads has been reduced by over 25% due to higher power density in the oscillating beam set-up. Most of the clads of brittle alloys developed transverse cracks probably due to high thermal stresses resulting from rapid solidification. It was observed that cracking reduces with increase in clad width to thickness ratio. Few clads entirely free of cracks were produced from 3Ti and 6Ti alloys by controlling this aspect ratio. Alloys 0B, 0.5B and 1.0B have different bulk chemistry even though initial powder mixture composition was same for all. Variation in microhardness along the clad length of 1.5Hf alloy also indicates composition variation. Nozzle to substrate distance, powder carrier and shielding
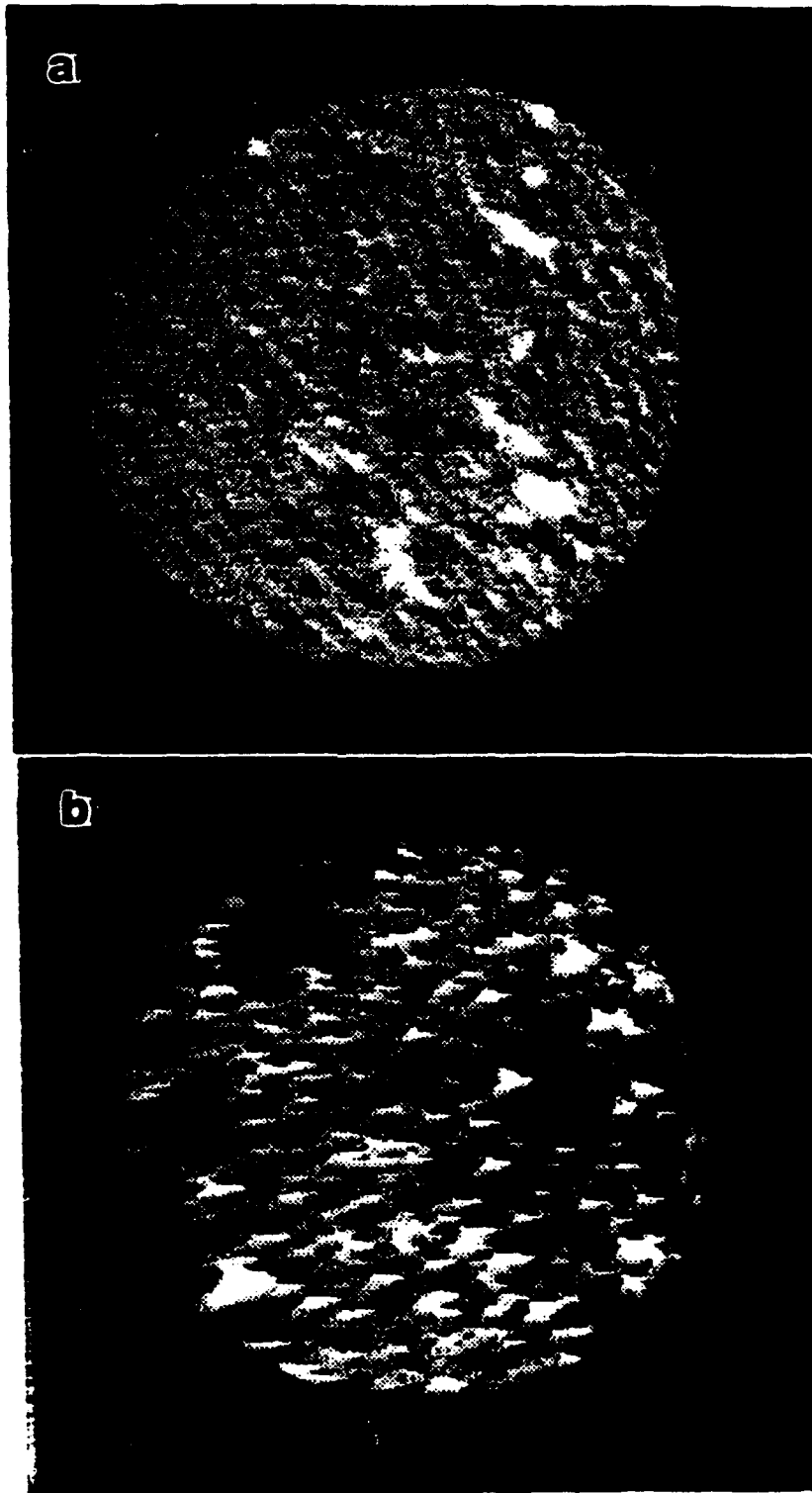
Figure-17 SIMS images of (a) B⁻, and (b) O_2^- in laser clad alloy 1.0B.

gas velocity, particle size and shape of powders used and depth of penetration are only few of the parameters affecting the final clad composition. Composition control is critical. This may be ensured by using pre-alloyed powder(which may not be readily available for experimental alloys). Mechanically alloying the powders or using powders of uniform size & shape and controlling the gas pressure during cladding are suitable alternatives at experimental stage. An on-line method of controlling the clad composition based on metal ion concentration in the laser plasma, obtained by optical emission spectroscopy, during cladding needs to be developed to solve this problem effectively.

Isothermal oxidation results at 1200°C indicate that alloys based on $NbAl_3$ only have adequate resistance. Although addition of 2.5 at% C improved the ductility of $NbAl_3$, oxidation resistance deteriorated. None of the Nb-rich Nb-Al alloys have good oxidation resistance. Further discussion is therefore confined to 0B, 0.5B, 1.0B, 3Ti, 6Ti and 1.5Hf alloys.

Clads of these alloys solidified with eutectic microstructure. Primary dendrites based on $NbAl_3$ extending almost perpendicularly from the interface into the clad is the major phase. Very fine eutectic forms in the 30-50μm layer at the interface with Nb_2Al based phase as the major constituent. Above this layer the microstructure is fairly uniform for all the alloys. Bulk chemistry indicates that 0B and 0.5B alloys contained Al less than, and 1.0B alloy more than, that for stoichiometric $NbAl_3$. Therefore, no Nb_2Al in 1.0B alloy, and no Al-rich phase in 0.5B alloy, must be present as per the equilibrium Nb-Al phase diagram. However, these phases are present in very small amount. Nb_2Al present in 0B, 0.5B and 1.0B alloys has composition conforming to that in equilibrium with $NbAl_3$ and not of the stoichiometric Nb_2Al as indicated from the EDX results. SEM and EDX results indicate that abo 1.4 at% Ti replaced Nb in $NbAl_3$ in 3Ti and 6Ti alloys. The dark interdendritic phase appears to be $(Nb,Ti)Al_3$ with about equal proportions of Nb and Ti. About 0.6 at%(in the center of the clad) to 1.4 at%(near interface) Hf replaced mostly Nb in $NbAl_3$ in 1.5Hf alloy and the dark Al-rich interdendritic phase contains about 2.2 at% Hf. Very small amount of Nb_2Al based white

phase is present in 3Ti, 6Ti and 1.5Hf alloys. Presence of Al-rich phase in 0.5B, 1.0B and 1.5Hf alloys is corroborated from the endothermic phase transformation observed near 650°C during heating runs.

The microhardness values measured for 0B, 0.5B and 1.0B alloys are close to that reported in literature(26) for $NbAl_3$. Hardness indentations for 3Ti, 6Ti and 1.5Hf alloys show very little or no cracking indicating improvement in ductility. From isothermal oxidation test results at 800, 1200 and 1400°C in air it can be seen that small additions of B have no adverse effect, and 1.5 at% Hf and upto 6 at% Ti improve the oxidation resistance of $NbAl_3$. Addition of Ti may promote external alumina scale formation by 'gettering' effect or/and by increasing the solubility-diffusivity product of Al(5). Hf additions may reduce the solubility-diffusivity product of oxygen in the alloy(25) and improve oxidation resistance. Hf additions may also improve alumina scale adherence as in the case of Ni-base superalloys. Alloys containing aluminum rich phase appear to have better oxidation resistance. However, its effect on the mechanical properties at the service temperature must be evaluated. Since this interdendritic Al-rich phase does not appear to be continuous it may not result into catastrophic failure at low stresses.

Value of parabolic rate constant for isothermal oxidation at 1200°C in air for 0.5B, 1.0B, 3Ti, 6Ti and 1.5Hf alloys are comparable to that reported in literature(8) for $Nb_{24}Al_{67}Cr_7Si_{1.5}Y_{0.5}$ alloy which forms alumina under similar conditions. The value for alloy 6Ti is 2-3 orders of magnitude better than that for a similar alloy(8). In our alloy Ti replaced Nb and not Al as was done in the previous study. The values of parabolic rate constant for isothermal oxidation in air at 1400°C for all the alloys is comparable to or better than that for alloy $Nb_{25.4}Ti_{29.1}Cr_{2.8}V_{3.5}Al_{39.2}$ developed by Perkins et. al.(5).

Most of the samples of 0B alloy isothermally oxidized in air at 800°C crumbled into black powder probably due to 'pest' phenomenon and those oxidized at 1200 and 1400°C cracked into pieces. This was not observed for other alloys for any of the three test conditions. This may be due to very low amount of interdendritic Nb_2Al which oxidizes faster than $NbAl_3$ or presence of Al-rich phases

in these alloys. Samples of 0.5B and 1.0B formed a uniform external layer of α-alumina when oxidized in air at 800, 1200 and 1400°C as observed from XRD and SEM/EDX results. Previous studies suggest that alumina forms only at 1400°C. Nb_2Al present in the alloys oxidizes forming $NbAlO_4$, which remains embedded in the alumina layer as seen clearly in figures-14(b), (d) and (e). Deeper penetration at the sites where Nb_2Al existed suggests that its oxidation occurs at a faster rate. $NbAl_3$ does not oxidize forming alternating layers of alumina and $NbAlO_4$ as reported in literature (4, 5, 29). The difference may be due to presence of B in our alloys. SIMS results indicate(figure-17(a)) that B is not uniformly distributed in 0.5B and 1.0B alloys. However, in which phase or area B is segregated and its effect on oxidation can not be determined from the available data. This needs to be investigated further. A layer of Nb_2Al formed below alumina layer in alloys 0.5B and 1.0B oxidized at 1200 and 1400°C in air only in regions where Nb_2Al is present in significant amount in the unoxidized sample. The pre-existing Nb_2Al in the sample is continuous with the newly formed Nb_2Al(figures-14(b), (c) &(e)) below alumina. This suggests that presence of Nb_2Al assists its precipitation below the oxide layer. The Nb_2Al layer below alumina remains unoxidized. This suggests that oxidation of 0.5B and 1.0B alloys at 1200 and 1400°C in air occurs by outward diffusion of aluminum(through Nb_2Al), and not by inward diffusion of oxygen. It also suggests that the equilibrium partial pressure of oxygen established below the alumina layer is insufficient for the oxidation of Nb_2Al into $NbAlO_4$. Sample of 0B alloy isothermally oxidized at 800°C in air formed a mixture of Al_2O_3 and $NbAlO_4$ oxides, black in color, which cracked extensively as seen in figure-12(a). The cracking could be due to thermal expansion or/and oxide to metal volume ratio mismatch. EDX analysis of the primary dendrite just below the oxide layer showed that its composition is same as that of the primary $NbAl_3$ dendrites in 0.5B and 1.0B alloys. Then why exclusive layer of alumina forms on the $NbAl_3$ dendrites in 0.5B and 1.0B alloys and not in 0B alloy oxidized at 800°C in air? Alloy 0B contains considerably larger amount of Nb_2Al phase than the other two alloys. This suggests that presence of Nb_2Al in significant amount may

reduce the chemical activity of Al in the alloy compared to that in relatively pure NbAl$_3$. Thermodynamic evidence is required to confirm this hypothesis. Alumina did form on samples of 0B alloy oxidized in air at 1200 and 1400°C as observed from the SEM/EDX analysis of the broken samples. Change in slope of the logk$_p$ vs 1/T graphs(figure-5) indicates that different oxidation mechanisms may be operating in the temperature regimes, 800-1200°C and 1200-1400°C for all the alloys. Tests at intermediate temperatures and with varying partial pressures of oxygen are needed to identify the mechanisms involved.

1.6 CONCLUSIONS

The process and parameters for laser processing have been established. Laser clad alloys 0.5B(Nb$_{25}$Al$_{74.5}$B$_{0.5}$), 1.0B(Nb$_{25}$Al$_{74}$B$_{1.0}$), 3Ti(Nb$_{22}$Al$_{74}$Ti$_3$B$_{1.0}$), 6Ti(Nb$_{19}$Al$_{74}$Ti$_6$B$_{1.0}$) and 1.5Hf(Nb$_{25}$Al$_{74.5}$Hf$_{1.5}$) oxidize with parabolic kinetics during isothermal oxidation in air at 800, 1200 and 1400°C. Parabolic rate constants comparable to β-NiAl(27), isothermally oxidized in 0.1atm. oxygen, are obtained at 1200° and 1400°C for all these alloys. At 800°C all the alloys have parabolic rate constant about 3 to 4 orders of magnitude higher than that for β-NiAl (extrapolated data at 800°C from ref. 27). This may be due to several reasons; differences in the oxidizing environment, higher rate of transient oxidation in our alloys or invalidity of the extrapolated data for β-NiAl at 800°C. NbAl$_3$ is the major phase present in these alloys. Boron is non-uniformly distributed in 0.5B and 1.0B alloys. About 1.4 at% Ti and 0.6 to 1.4 at% Hf replaces Nb in NbAl$_3$ in 3Ti & 6Ti and 1.5Hf alloys, respectively. Interdendritic phase based on Nb$_2$Al is present in all the alloys. In addition, an aluminum rich phase in 0.5B, 1.0B and 1.5Hf alloys and (Nb,Ti)Al$_3$ phase in 3Ti and 6Ti alloys is also present at interdendritic region. External layer of alumina forms on 0.5B and 1.0B alloys at 800, 1200 and 1400°C in air and oxidation occurs by outward diffusion of aluminum. No alternating layers of alumina and NbAlO$_4$ form in any of the samples as reported in literature for oxidation of NbAl$_3$. A layer of Nb$_2$Al forms at 1200 and 1400°C below

the alumina layer only in regions where Nb_2Al is present in significant amount in the unoxidized 0.5B and 1.0B alloys. This Nb_2Al remained unoxidized. Presence of significant amount of Nb_2Al in 0B alloy may be responsible for the formation of a mixture of alumina and $NbAlO_4$ rather than only alumina at 800°C in air. Addition of upto 1.0at%B has no adverse effect on the oxidation resistance of $NbAl_3$. Isothermal oxidation resistance of $NbAl_3$ at 800, 1200 and 1400°C in air is improved by, addition of upto 6at% Ti(replacing Nb), probably, due to increase in the solubility-diffusivity product of Al, and by addition of 1.5at% Hf, probably, due to decrease in solubility-diffusivity product of oxygen. Additions of 1.0at%B, 3at%Ti, and 1.5at%Hf to $NbAl_3$ may improve its ductility.

1.7 MATHEMATICAL MODELING

1.7.1 Theoretical Studies on Nonequilibrium Phase Diagram for Nb-Al Alloy Formed during Laser Cladding

A one dimensional finite-medium diffusion model earlier developed in this group(30, 31) for dilute solutions is used to study the effect of various process parameters on the composition of solid solution in laser clad binary Nb-Al alloy. Mathematical formulation, physical assumptions and solution of the model are described in references 30 and 31. The model considers concentration dependent freezing point and nonequilibrium partitioning of solute at the solid-liquid interface. The predicted concentration of Al in the extended solid solution of Nb-Al binary system is found to compare well with experimental data. The proposed nonequilibrium phase diagram for Nb-Al system, near the compound $NbAl_3$, based on predictions of the model explains the experimentally observed distribution of Al in the clad. Important results of this investigation are briefly described below. Results of this study are presented in detail in a paper(32) submitted for publication in Acta. Met. et Materialia.

Experimental results obtained for 0B alloy produced using 6 kW laser power with 4 x 4.5 mm spot size, 9.3 mm/s substrate velocity, and 0.178 gm/s powder feed rate were used to verify the

prediction of the model. Bulk chemical analysis of a sample from this clad indicated concentration of Al to be 40.63 wt% instead of aimed 50.05 wt%. Details of microstructure are already described in section 1.4.3 in this report. The model predicts 39.48 wt % Al in the bulk which compares well with the experimental data. Initial mean temperature of clad melt pool obtained from energy balance is estimated to be 1608 °C.

Equilibrium Nb-Al phase diagram(33) in the vicinity of compound $NbAl_3$ is presented in figure-18 along with the theoretical nonequilibrium phase diagram obtained from this model. Calculated nonequilibrium liquidus and solidus curves for three powder feed rates are shown in this figure. Nonequilibrium curves for powder feed rate 0.178 gm/s correspond to clads obtained using experimental conditions described above. It is important to note that the nonequilibrium curves for different combinations of process parameters do not coincide. The metastable compositions that result after the laser cladding process are very sensitive to the given interaction time. This physical parameter embodies both, the kinetic as well as energetic driving force for the metastable compositions to attain equilibrium. In figure-18, the nonequilibrium curves are plotted for different cladding powder feed rates which are directly proportional to the workpiece speed. Interaction time, defined as the ratio of the effective laser beam diameter to the substrate speed, maintains a similar proportionality to the feed rate. Intuitively, therefore one would expect the difference from the equilibrium curve to decrease with increase in interaction time. This can be verified from the curves. The nonequilibrium solidus line shows that an extension of niobium in the Nb-Al alloy can be obtained. Excess aluminum is relegated to the liquid phase. Therefore, one would expect the concentration of aluminum in the liquid phase to be greater than the equilibrium concentration, as was the case in Ni-Al system (31). Since the liquidus concentration represents the interface composition, one possible explanation for the same could be that aluminum is rapidly diffusing away from interface to form an Al - rich phase at the top of the cladding. This explanation conforms with
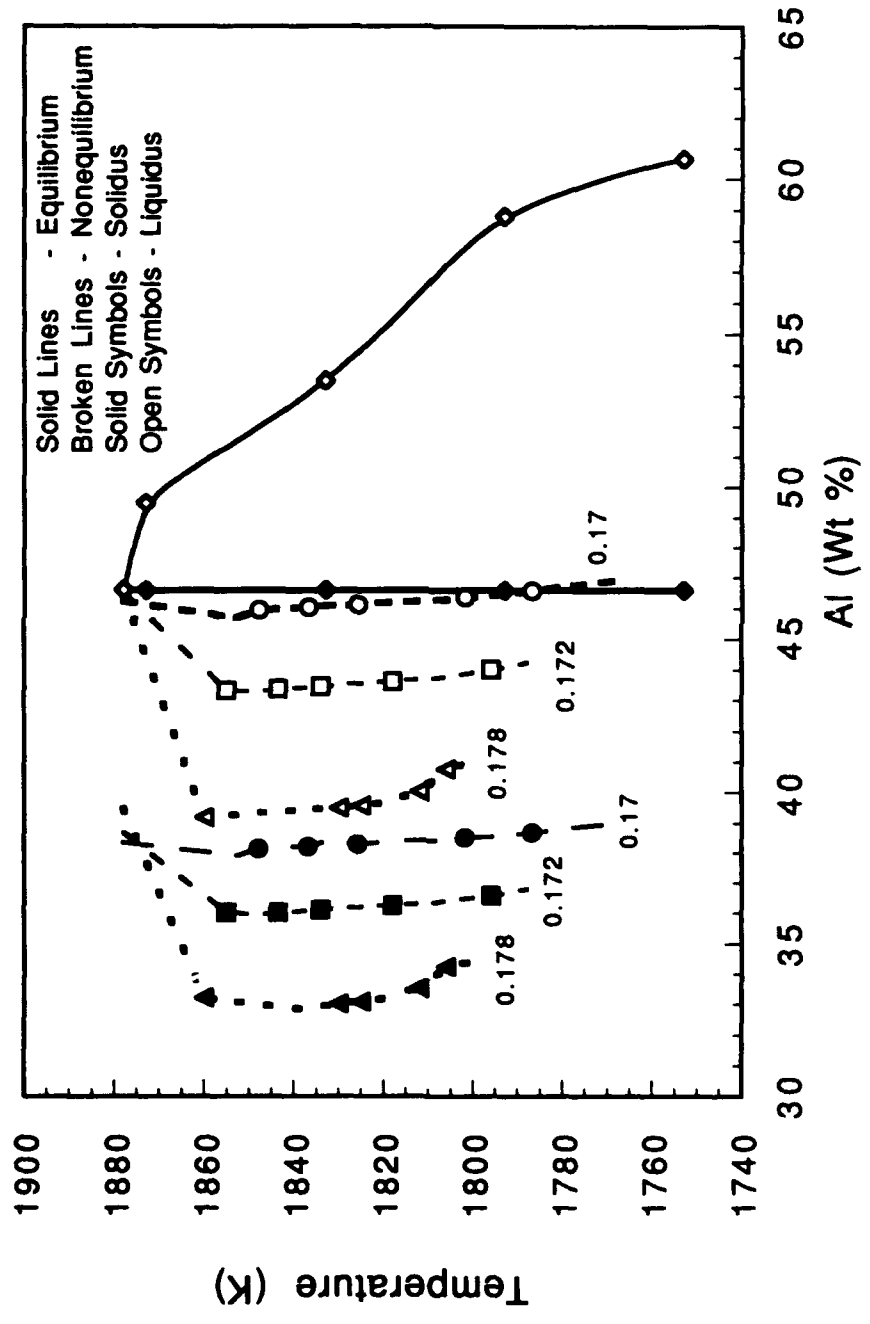
Figure-18 Equilibrium(33) and nonequilibrium Nb-Al phase diagram in the vicinity of NbAl$_3$. Numbers below lines represent powder feed rate in gm/s.

the experimental results where the top surface of clad is rich in aluminum indicating a preferential segregation.

1.7.2 Nonequilibrium Partition Coefficient for Binary Concentrated Solutions

Inherent rapid solidification during laser cladding invariably produces novel materials due to nonequilibrium segregation of solute atoms. Using kinetic model of nonequilibrium solidification, several studies have already been carried out under dilute solution approximation to derive an expression for nonequilibrium partition coefficient. However, these models are not valid for concentrated solutions frequently encountered in laser cladding and alloying processes. A model for nonequilibrium partitioning of solute in binary concentrated solutions is developed(34), to obtain an expression for nonequilibrium partition coefficient with only one unknown parameter. The modified nonequilibrium partition coefficient ($k_m = m_s/m_l$) for concentrated solutions is given by the following expression

$$k_m = \frac{k_m^* + \beta}{1 + \beta}$$

where, $\beta = u\lambda/D_{ABs}$ is defined as dimensionless solidification rate.

The symbols used in the above equation are defined below:

D_{ABs} Interdiffusion coefficient of species A with respect to species B in the solid phase.

k_m^* Modified equilibrium partition coefficient for concentrated solutions ($= m_s^*/m_l^*$).

m_l Reciprocal of the liquidus slope at temperature T_i.

m_s Reciprocal of the solidus slope at temperature T_i.

m_l^* Reciprocal of the liquidus slope at the solidification temperature (T_i) under equilibrium cooling condition.

m_s^* Reciprocal of the solidus slope at the solidification temperature (T_i) under equilibrium cooling condition.

T_i Interface temperature.

u   Speed of the freezing front.

λ Characteristic length for diffusion.

Salient features of the model are briefly described below. Details of the model can be obtained from paper in Ref. 34. Although there are several expressions for nonequilibrium partition coefficient (NPC) for dilute solutions, there is only one expression (35, 36) for NPC for concentrated solutions in the available literature. One has to determine several parameters and then solve a transcendental equation to obtain the NPC for concentrated solutions, if one chooses to use the expression given in Refs. (35, 36). The purpose of our work is to provide an expression for NPC for concentrated solutions with fewer unknown parameters. If the characteristic velocity(D_{ABs}/λ) is considered as an adjustable parameter, the NPC for concentrated solutions can be determined solely by using the equilibrium phase diagrams, because our expression for NPC has only one unknown parameter. It should be noted that lack of any experimental data over an extended range of regrowth velocities is also a severe limitation on theory-experiment comparisons. For this reason the values of NPC obtained from our model have not been compared with any experimental data due to the unavailability of such data for concentrated solutions. Instead, besides deriving the expression for NPC on the basis of a model, it has also been derived directly from mathematical considerations in order to check if the same expression can be obtained by using two entirely different approaches.

Since our expression for NPC for concentrated solutions has only one adjustable parameter, it provides experimental solidification researchers an easier alternative to estimate extended solid solubility and generate nonequilibrium phase diagrams of rapidly solidified alloys of concentrated solutions.

2. LASER CLADDING OF NiAlCr ALLOYS CONTAINING Hf

NiAlCr alloy coatings are widely used at elevated temperatures for protection of Ni-base superalloys from oxidation. Retention of alumina scale formed on these alloys during cyclic oxidation is enhanced by minor additions of rare-earth reactive elements. This study was carried out to understand the mechanism by which Hf, a rare-earth element, improves the adherence of alumina scale in laser clad NiAlCrHf alloy during cyclic oxidation in air. Advantages of laser cladding over conventional processing methods are also investigated.

Coating of $Ni_{70}Al_{20}Cr_7Hf_3$ alloy with extended solid solubility of Hf were successfully produced by laser cladding on a commercial Ni-base superalloy Rene 80. Laser clad alloy exhibited isothermal and cyclic oxidation resistance at 1200°C in air superior to that of Rene 80. Alumina scale formed on laser clad alloy remained strongly adherent to the base alloy. This was believed to be due to spikes of hafnia extending into the base alloy from the alumina-hafnia scale. However, the rate of isothermal oxidation was about half an order of magnitude higher than that for similar alloy produced by conventional non-consumable arc melting process. This was attributed to presence of large number of undissolved Hf particles and formation of interdendritic Hf-rich phase in the laser clad alloy containing 3at%(10wt%) Hf, limiting its potential for application. Therefore, it was concluded that optimizing the Hf content while maintaining solid solubility extension is critical in the development of cladding alloys with good oxidation resistance. The details of the experiments and the results obtained are described in detail in earlier report(1).

NiAlCr alloys containing 0, 1 and 3wt% Hf (nominal) representing the conditions of no Hf, an amount approximately equal to the equilibrium solubility and an amount significantly greater than the equilibrium solubility, respectively, were produced by laser cladding on commercially pure Ni (Ni200) substrates. Use of pure Ni substrates eliminated the possibility of contamination of clads by alloying elements present in Rene 80 which might have affected the oxidation results and complicated the analysis.

It was demonstrated through calculations that alumina scale grown at 1200°C in air on Ni-base alloys spalls of during cooling due to compressive stresses generated by the constraints by the underlying metal. It was found that additions of up to at least about 2.5Wt% Hf improve the cyclic oxidation resistance of alumina forming NiAlCr alloys in air at 1200°C. Laser clad alloys were superior to arc melted. Samples of laser clad alloy containing about 2.5Wt% Hf retained almost completely intact scale. It was proposed that improvement in adherence results from toughening of the equiaxed alumina scale due to microcracking induced by anisotropic thermal extension of the hafnia polycrystallites. Micro-cracking toughening is enhanced by increase in the number density of hafnia polycrystallites in the scale. Compared to arc melted alloys finer Hf-rich particles($\approx 1 \mu m$) in higher number density were more uniformly distributed in laser clad alloy with finer microstructure. Since these particles are precursors to the hafnia in the scale responsible for toughening and improved adherence of alumina, laser clad alloys are superior. Laser cladding parameters did not have measurable effect on the oxidation response of the alloys.

A new mechanism of improvement in alumina scale retention was proposed and the advantages of laser cladding were identified. The details of experiments and results obtained are described in earlier report(2) and a paper accepted for publication in Met. Trans. B (attached as Appendix B).

3. LASER CLADDING OF Mg-BASE ALLOYS

Magnesium alloys with low density and superb machinability have limited applications as engineering materials due to poor corrosion resistance. In this study efforts were made to produce corrosion resistant Mg-Al alloys with minor additions of Ce or Zr by laser cladding technique.

Laser cladding process was developed to produce oxidation free clads of Mg-rich and Al-rich Mg-Al alloys with and without minor additions of Ce or Zr. Cladding was done in a specially designed chamber under protective inert atmosphere above ambient pressure in order to avoid oxidation. This also helped in minimizing loss of Mg by evaporation because of its high vapor pressure. Alloys $Mg_{72}Al_{23}$, $Mg_{53}Al_{47}$, $Mg_{27}Al_{73}$, $Mg_{27}Al_{72.9}Zr_{0.1}$, $Mg_{26.9}Al_{72.8}Zr_{0.3}$, $Mg_{26.2}Al_{70.9}Ce_{2.9}$ and $Mg_{26.9}Al_{72.8}Ce_{0.3}$ were produced by laser cladding. Differential Thermal Analysis of the clads was carried out to study the phase transformations. Microstructure of the clads was examined in detail and correlated with the laser cladding parameters. Corrosion resistance of the clads was determined from Potentiodynamic Anodic Polarization, Corrosion Potential(E_{corr}), Tafel Plot and Polarization Resistance tests.

Microexamination of the clads indicated that amount of phases present in these alloys is affected by the specific energy input during laser cladding. $Mg_{27}Al_{73}$ had the best corrosion resistance in 3.5wt% NaCl solution among all the laser clad alloys studied and is superior to commercial Mg alloy AZ91B and cast Mg.

The results of the investigation are described in detail in earlier reports(1, 2).

4. ACKNOWLEDGEMENTS

5. REFERENCES

1. J. Mazumder et al., Annual Progress Report, AFOSR Project 89-0061, 1989.
2. J. Mazumder et al., Annual Progress Report, AFOSR Project 89-0061, 1991.
3. R. C. Svedberg, Properties of High Temperature Alloys, eds. Z. A. Foroulis & F. S. Pettit, Electrochem. Soc., 33, 1976.
4. R. A. Perkins, K. T. Chiang & G. H. Meier, Scripta. Met., Vol. 21, 1505, 1987.
5. R. A. Perkins, K. T. Chiang & G. H. Meier, Scripta. Met., Vol. 22, 419, 1988.
6. C. Wagner, Z. Electrochem., 63, 772 1959.
7. C. Wagner, Corrosion Sc., Vol. 5, 751, 1965.
8. M. G. Hebsur, J. R. Stephens, J. L. Smialek, C. A. Barrett & D. S. Fox, Oxidation of High Temperature Intermetallics, Eds. T. Gorbstein & J. Doychak, The Minerals, Metals & Materials Soc., 171, 1989.
9. M. Steinhorst & H. J. Garbke, Mat. Sc. & Engg., A120, 55, 1989.
10. H. J. Garbke, M. Steinhorst, M. Brumm & D. Wiemer, Oxidation of Metals, Vol. 35, 199, 1991.
11. D. Schechtman & L. A. Jacobson, Met. Trans. A, Vol. 6A, 1325, July 1975.
12. O. Izumi & T. Takasugi, J. Mater. Res., 3(3), 426, May/June 1988.
13. Alloys of Niobium, ed. A. M. Samarin, Israel Program of Scientific Translations, Jerusalem, p. 47, 1965.
14. P. R. Subramanian, J. P. Simmons, M. G. Mendiratta & D. M. Dimiduk, High Temperature Ordered Intermetallic Alloys III, ed.C. T. Liu, A. I. Taub, N. S. Stoloff, C. C. Koch, MRS 1989.
15. D. G. Pettifor, J. Phys. C., 19, 285, 1986.
16. A. Raman & K. Schubert, Z. Metallk., 56, 40, 99, 1965.
17. P. Virdis & U. Zwicker, Z. Metallk., 62, 46, 1971.
18. A. Seibold, Z. Metallk., 27, 177, 1987.
19. A. E. Carlsson & P. J. Meschter, J. Mat. Res., vol. 5, No. 12, 2813, Dec. 1990.
20. J. Singh and J. Mazumder, Mat. Sc. Technol., Vol. 2, 709, 1986.
21. J. Singh and J. Mazumder, Met. Trans. A, Vol. 18A, 313, 1987.

22. L. J. Li and J. Mazumder, in Laser Processing of Materials, eds. K. Mukherjee and J. Mazumder, 35-50, TMS-AIME 1985.
23. T. Chande and J. Mazumder, Appl. Phys. Let., Vol. 41, 42, 1982.
24. T. Chande and J. Mazumder, J. Appl. phys., Vol. 57, 2226, 1985.
25. D. L. Corn, D. L. Douglas & C. A. Smith, Oxidation of Metals, Vol. 35 139, 1991.
26. B. Pieraggi, Oxidation of Metals, Vol. 27, 177, 1987.
27. F.S. Pettit, Trans. AIME, Vol. 239, 1296, 1967.
28. R. L. Fleischer, Mater. Res. Soc. Symp. Proc., Vol. 133, 305 1989.
29. R. A. Perkins, K. T. Chiang, G. H. Meier & R. Miller, Oxidation of High Temperature Intermetallics, Eds. T. Gorbstein & J. Doychak, The Minerals, Metals & Materials Soc., 157, 1989.
30. A. Kar and J. Mazumder, Acta Metall., 36, 701, 1988.
31. A. Kar and J. Mazumder, Metall. Trans. A, 20A, 363, 1989.
32. G. Agrawal, A. Kar and J. Mazumder,Submitted for publication in Acta. Met. et Materialia.
33. Bulletin of Alloy Phase Diagrams, 2, 75, 1981.
34. A. Kar and J. Mazumder, Accepted for publication in Acta Metall. et Materialia.
35. M. J. Aziz, Appl. Phys. Lett., 43, 552,1983.
36. M. J. Aziz, in Science and Technology of Rapidly Quenched Alloys, edited by M. Tenhover, W. L. Johnson, and L. E. Tanner (Materials Research Society, Pittsburgh, PA, 1987), p. 25.

6. APPENDIX A

List of Publications (during the contract period for AFOSR 89-0061, Nov. 88 to date)

1. "Laser Cladding of Zr on Mg for Improved Corrosion Properties," *Proc. of Environmental Degradation of Ion and Laser Beam Treated Surfaces*, G. S. Was and K. S. Grabowski (eds.), published by TMS-AIME, pp. 59-70, 1988 (with S. Raja and J. Singh).

2. "Extended Solid Solution and Nonequilibrium Phase Diagram for Ni-Al Alloy Formed during Laser Cladding," *Met. Trans. A*, Vol. 20A, pp. 363-371, March 1989 (with A. Kar).

3. "New Materials: Non Equilibrium Synthesis by Laser," *J. of Laser Applications*, Vol. 1, No. 2, pp. 27-42, March 1989 (with S. Sircar, C. Ribaudo, and A. Kar).

4. "Laser Cladding of Zr on Mg for Improved Corrosion Properties," accepted for publication, *J. of Materials Science*, Vol. 26, pp. 951-956, 1991 (with R. Subramanian and S. Sircar).

5. "Oxidation Behavior of a Laser-Clad Nickel-Based Alloy Containing Hafnium," *Materials Science and Engineering*, Vol. A121, pp. 531-538, 1989 (with C. Ribaudo).

6. "Laser Clad $Ni_{70}Al_{20}Cr_7Hf_3$ with Extended Solid Solution of Hf: Part I: Microstructure Evolution," *Metallurgical Transactions*, Vol. 20A, No. 11, pp. 2267-2277, 1989 (with S. Sircar and C. Ribaudo).

7. "Laser Clad $Ni_{70}Al_{20}Cr_7Hf_3$ with Extended Solid Solution of Hf: Part II: Oxidation Behavior," *Metallurgical Transactions*, Vol. 20A, No. 11, pp. 2489-2497, 1989 (with S. Sircar and C. Ribaudo).

8. "Microstructure Evolution and Nonequilibrium Phase Diagram for Ni-Hf Binary Alloy Produced by Laser Cladding," *Acta Metallurgica*, Vol. 37, No. 4, pp. 1167-1176, 1989 (with S. Sircar and J. Singh).

9. "Laser Cladding of Mg-Al Alloys," accepted for publication by *J. of Materials Science* (with A. Wang and S. Sircar).

10. "Nonequilibrium Synthesis of NbAl$_3$ & Nb-Al-V Alloys by Laser Cladding, Part I: Microstructure Evolution," accepted for publication in *Metallurgical Transactions A* (with S. Sircar and K. Chattopadhyay).

11. "Nonequilibrium Synthesis of NbAl$_3$ & Nb-Al-V Alloys by Laser Cladding, Part II: Oxidation Properties," accepted for publication in *Metallurgical Transactions A* (with R. Haasch, S. Tewari, S. Sircar and C. Loxton).

12. "Laser Clad NiAlCrHf Alloys with Improved Alumina Scale Retention," accepted for publication in *Metallurgical Transactions*, June 1991 (with C. R. Ribaudo and D. W. Hetzner).

13. "Model for Nonequilibrium Partitioning during Rapid Solidification of Concentrated Solution," accepted for publication in *Acta Metallurgica* (with A. Kar).

14. "Theoretical Studies on Extended Solid Solubility and Nonequilibrium Phase Diagram for Nb-Al Alloy Formed during Laser Cladding," submitted to *Acta Metallurgica et Materialia*, Jan. 1992 (with G. Agrawal and A. Kar).

15. "Non-Equilibrium Synthesis of Alloys using Lasers," invited presentation at ISATA '90, Nov. 1990, Turin, Italy (with J. Choi, C. Ribaudo, A. Wang and A. Kar).

7. APPENDIX B

"Laser Clad NiAlCrHf Alloys with Improved Alumina Scale Retention,"

by

C. R. Ribaudo, J. Mazumder, and D. W. Hetzner.

LASER CLAD NiAlCrHf ALLOYS WITH IMPROVED ALUMINA SCALE RETENTION

Carl R. Ribaudo*, Jyoti Mazumder**

Center for Laser Aided Materials Processing
Department of Mechanical and Industrial Engineering
University of Illinois at Urbana-Champaign
1206 West Green Street
Urbana, IL 61801

Dennis W. Hetzner***
The Timken Company
1835 Dueber Ave SW
Canton, OH 44706

A new mechanism for the improved retention of alumina scales formed on laser clad NiAlCrHf alloys has been observed. Laser cladding is the process where fine metal powders are rapidly melted and fused to a solid substrate using a CO_2 laser. The effects of laser cladding upon scale retention on NiAlCrHf alloys after cyclic and isothermal exposure to air were investigated using thermogravimetric analysis (TGA), x-ray diffraction (XRD), and scanning electron microscopy (SEM). The calculated compressive stress in the scale due to constrained cooling exceeded the probable compressive strength of alumina. Additions of up to ≈ 2 1/2 w/o Hf increasingly promote retention of scales grown at 1200°C with laser clad samples of ≈ 2 1/2 w/o Hf alloy retaining almost completely intact scales. The improvement in scale retention is due to improved toughness in scales containing hafnia polycrystallites possibly via microcracking initiated by anisotropic thermal contraction of the hafnia. Laser cladding the 2 1/2 w/o Hf alloy provides a large concentration of ≈ 1μm Hf-rich particles that are precursors of the hafnia in the scale as well as a finer dendrite spacing that reduces the mean free distance between particles.

---

* Principal Research Engineer, The Timken Co., Canton, OH, formerly Graduate Research Assistant, Dept. of Materials Science and Engineering
** Professor of Mechanical Engineering and Materials Engineering
*** Research Specialist

I. Introduction

As noted earlier,[1] α-alumina scales are protective on NiAlCr alloys exposed to high temperature oxidation, but poor retention of the alumina during thermal cycling is often observed. Additions of reactive elements (RE's), those elements in Columns IIIA and IVA of the periodic table, to alumina-forming alloys are commercially employed to improve scale retention. Several mechanisms have been proposed to explain the beneficial effect of RE's, but no consensus has been reached as to which mechanism(s) are active.[2,3] These mechanisms assume that scale spallation is either caused by a lack of adherence because the scale-metal interface is inherently weak or by a lack of coherence due to a deficiency in the mechanical properties of the scale itself as listed in Table I.

Table I Reactive Element Effects upon Alumina Scale Retention

Adherence Mechanisms	Coherence Mechanisms
Mechanical Pegging[4]	Graded Seal[11]
Vacancy Sinks[5]	Improved Scale Plasticity via Grain Boundary Sliding[12]
Sulfur Segregation[6-10]	Growth Mechanism Alteration[12]
	Stress Relief[13]

Luthra and Briant suggested that stress relief observed in scales formed on NiCrAlY and NiCoCrAlY alloys may be caused by a mechanism not previously reported and further hypothesized that this might occur by microcracking in the scale.[13]

Laser cladding may enhance the ability of RE's to produce tenacious alumina scales. The process consists of melting a pneumatically injected mixture of mechanically blended metallic powders and a limited amount of substrate with a high power laser to produce a cladment with

less than 20 % dilution that is metallurgically bonded to the substrate. Rapid cooling rates produced in this process result in a fine microstructure and an extension of the solid solubility of Hf in NiAlCr alloys.[14] Both of these features serve to further disperse the RE's with the possibility of enhancing alumina scale retention.

Laser clad NiAlCrHf alloys with good scale retention were produced earlier at the cost of excessive isothermal weight gains.[1] No significant spalling from samples containing about 10 w/o Hf was observed during 24 cycles between ambient and 1200°C in air. The weight gains measured using thermogravimetric analysis (TGA) were about an order of magnitude higher than those given in the literature for alumina-forming NiAlCr alloys[15,16] due to the oxidation of a large number of partially unmelted Hf powder particles and an eutectic constituent containing ~ 58 w/o Hf .[14]

This work centers upon determining the effects of laser cladding and Hf additions upon the oxidation behavior of NiAlCr alloys, especially with regard to scale retention. Two levels of Hf were added to a base alloy with the higher level approximately 1/4 of that in the earlier alloy.

II. Experimental Procedure

The cladding process used previously[1] was modified by using an integrating mirror to produce a more uniform laser beam and by replacing the commercial superalloy substrate with Ni 200, a commercially pure Ni. Values of the laser cladding parameters are given in Table II. The compositions of the alloys tested are given in Table III.

Buttons of 50 to 75 grams were also fused from each of these powder mixtures using a non-consummable electrode. The melting chamber was evacuated to 1.3 mPa and back filled with Ar prior to melting. The buttons were turned over and remelted to improve chemical homogeneity.

Table II Laser Cladding Parameters

Laser	AVCO HPL continuous wave CO_2
Laser Power	7.25 kw
Substrate Traverse Speed	5.5 mm/s
Powder Feed Rate	0.37 g/s
Beam	5 mm x 5 mm

Table III. Chemical Composition of Alloys Prepared

	Sample	Weight %				Weight ppm		
		Ni	Al	Cr	Hf	S	O	N
Arc	O w/o Hf	81.63	11.17	7.16	0.04	9	14	6
Laser	O w/o Hf	84.67	9.44	5.85	0.04	25	--	33
Arc	1w/o Hf	80.67	10.98	7.41	0.94	3	14	5
Laser	1w/o Hf	83.63	9.72	5.97	0.80	15	--	21
Arc	2 1/2 w/o Hf	79.91	10.60	6.97	2.52	7	11	7
Laser	2 1/2 w/o Hf	83.07	9.07	5.79	2.07	20	--	22

Oxidation resistance in slowly flowing air was measured using TGA. The sample was suspended from a quartz extension loop to reduce weight loss of the Pt hangdown wire via oxidation and volatilization while allowing for direct measurement of any scale spallation. Isothermal testing was performed by heating the samples at 1.7 °C/s and holding at 1000°C, 1100°C, or 1200°C for 20 hours and cooling at 0.17 °C/s to ambient. Cyclic testing consisted of heating at 1.7 °C/s, holding for one hour at 1000°C or 1200°C and cooling to about 50°C. The cooling rate was a function of temperature with an initial rate of about 0.7 °C/s. Samples approximately 1 mm x 2 mm x 5 mm were polished ending with the use of an aqueous suspension of 0.05 μm alumina. Swabbing with trichloroethane and acetone and ultrasonic cleaning in methanol completed the preparation.

Microstructural analysis of both as cast and oxidized samples was primarily performed using X-ray diffractometry (XRD) and scanning electron microscopy (SEM) techniques including energy dispersive X-ray analysis (EDS). The Hf content of various phases in the as-cast samples was measured using a scanning transmission electron microscope (STEM).[1] Measurement of the quantity and size distribution of Hf-rich phases in as-cast and oxidized 2 1/2 w/o Hf alloy was performed on twenty-five fields produced with a SEM at 2000X. The mean particle diameter and number density of these Hf-rich species was estimated using the Schwartz-Saltykov method.[17]

III. Results

A. Alloy Composition and Structure

Values for Al, Cr and Hf in the laser clad alloy given in Table III are 10 to 20% lower than those for the arc melted alloys due to dilution with the underlying substrate. Sulfur levels in the arc-melted alloys are about 1/3 of those in the laser clad samples.

The microstructure of the alloys was a function of both the processing method and Hf content. XRD results indicated the presence of γ' (ordered solid solution of type L12 with a $\approx$ 3.55Å) and σ (tetragonal solid solution of type tP30 with a = 8.86 to 8.90Å, c = 4.70 to 5.00Å, c/a = 0.529 to 0.562) in all of the samples. γ' dendrites were surrounded by γ of slightly higher Al content. Black rods of σ were found near the edges of some of the dendrites. Figure 1 shows that the laser clad alloys had a primary dendrite spacing of about 1/4 of that in the arc melted material. Laser clad 1 and 2 1/2 w/o Hf alloys also contained Hf-rich polygonal particles decorating the dendrites. These dispersoids are remnants of Hf powder particles partially melted during cladding.[14] Arc melted samples of 2 1/2 w/o Hf contain Hf-rich flakes produced during solidification. The flakes and particles are at least 90 w/o Hf. A higher number density (particles per unit volume) of Hf-rich particles is present in the laser clad alloy than of flakes in the arc melted material as shown in Table IV.

Table IV Hf-Rich Particles in Fused 2 1/2 w/o Hf Alloy

Process	No. of Particles Examined	10^6 Particles per mm^3	Median Length (μm)
Arc melted	338	2.81	1.38
Laser clad	565	10.5	0.52

B. Thermogravimetric Analysis (TGA)

Hf content dominates the isothermal oxidation response. Figure 2 displays the weight change per unit area as a function of the square root of time for isothermal exposure at 1200°C. Additions of 1 w/o Hf decrease the weight gain rate while additions of 2 1/2 w/o Hf increase this rate. During cooling, spallation was nearly complete on 0 w/o Hf alloy, and partial on 1 w/o Hf alloy while 2 1/2 w/o Hf alloy experienced little spallation. Results obtained at 1000°C and 1100°C were similar although spallation decreased on each alloy with decreasing temperature. Values of k_p, the parabolic rate constant, were computed as the square of the steady state slope[18] of plots such as those in Figure 2 and are presented in an Arrhenius plot in Figure 3. These results reasonably agree with data in the literature for NiAlCr alloys with alumina scales. [15,16]

Exceptions to this behavior were found for laser clad 0 w/o Hf and 1 w/o Hf alloys. Samples of 0 w/o Hf alloy suffered transverse cracking during the cladding process so that the weight change per unit surface area could not be accurately measured on most samples. Laser clad 1 w/o Hf alloy samples showed a maxima in k_p at 1100°C. While no clear explanation can be given for this behavior, similar results have been observed for other NiAlCr alloys.[16]

Cyclic oxidation resistance at 1200 °C was a strong function of Hf content and the interaction of Hf content and processing method. Figure 4a is a plot of the weight change (per unit area) of samples during cyclic oxidation. The 0 w/o Hf alloy samples spall during cooling from the first cycle and the spalling rate increases over time. 1 w/o Hf alloy suffers far less

weight loss and 2 1/2 w/o Hf alloy experienced almost no weight loss as shown in Figure 4a. The difference in the spalling rates in the 0 w/o and 1 w/o Hf alloys due to processing method is very small relative to the nominal spall rate. Expansion of the plot in Figure 4b of the results for the 2 1/2 w/o Hf alloy indicates that the laser clad samples continue to gain weight at an ever decreasing rate for up to 28 cycles while the arc-melted samples begin to spall and lose weight after about 10 to 15 cycles. Thus laser cladding improves the cyclic oxidation resistance of only the 2 1/2 w/o Hf alloy at 1200 °C.

Additional cyclic testing between 1000 °C and ambient indicated less influence of alloy composition or process method. Figure 5 shows that arc-melted 0 w/o Hf and 2 1/2 w/o Hf and laser clad 2 1/2 w/o Hf samples suffer no spallation through 20 cycles. While the amount of weight gained by the 0 w/o Hf alloy after 20 cycles (20 hours) at 1000 °C, 0.35 mg/cm^2, is roughly equal to that gained after 1 hour at 1200 °C (Figure 2a), measurable spallation did not occur in the former case and catastrophic spallation took place after the one hour at 1200°C.

C. Microanalysis of Oxidized Samples

The oxide phases retained on samples after cooling were primarily a function of hafnium concentration as shown in Table V. Scales containing α-Al$_2$O$_3$ and m-HfO$_2$ (monoclinic) were always grown and retained on the 2 1/2 w/o Hf alloy fused by either method.

The scale spallation on 0 Hf samples isothermally oxidized at 1200 °C indicated by TGA plots is confirmed by the micrographs shown in Figure 6. The polygonal relief network on the surface of the underlying arc-melted metal in (a) resembles the pattern of the grain boundaries found on the underside of spalled oxide flakes. The smooth fracture surface running perpendicular to the plane of the sample appears to result from the intergranular fracture of columnar oxide grain boundaries. EDS spectra taken from all faces of this flake indicate that they are very nearly pure alumina. Laser clad 0 w/o Hf samples produced very

similar results. As suggested by the TGA results, nearly intact alumina scales were found on the 0 w/o Hf samples after oxidation at 1000 °C.

Table V Phases Identified on Oxidized Samples Using XRD

Sample	1000 °C Isothermal (20 hours)	1200 °C Isothermal (20 hours)	1200 °C Cyclic (20 cycles)
Arc 0 w/o Hf	$\alpha\text{-}Al_2O3$	no oxides detected	$\alpha\text{-}Al_2O_3$ $NiAl_2O_4$ NiO
Laser 0 w/o Hf	NT	no oxides detected	NiO $NiAl_2O_4$
Arc 1w/o Hf	NT	$m\text{-}HfO_2$	$\alpha\text{-}Al_2O_3$ $NiAl_2O_4$
Laser 1w/o Hf	NT	$m\text{-}HfO_2$	no oxides detected
Arc 2 1/2 w/o Hf	$m\text{-}HfO_2$ $\alpha\text{-}Al_2O_3$	$m\text{-}HfO_2$ $\alpha\text{-}Al_2O_3$	$m\text{-}HfO_2$ $\alpha\text{-}Al_2O_3$
Laser 2 1/2 w/o Hf	$m\text{-}HfO_2$ $\alpha\text{-}Al_2O_3$ NiO $NiAl_2O_4$	$m\text{-}HfO_2$ $\alpha\text{-}Al_2O_3$	$m\text{-}HfO_2$ $\alpha\text{-}Al_2O_3$

NT = not tested

The addition of 1 w/o Hf produces a significant change in the morphology of the sample oxidized isothermally at 1200 °C as shown in Figure 7. A large number of small whitish particles were imbedded in the underlying laser clad alloy which are very rich in Hf and correspond to the m-HfO$_2$ discovered using XRD. While the fracture surface along the particle

appears to be mostly intergranular, the fracture steps in the upper righthand portion of the particle indicate that at least some transgranular fracture took place. Several other such particles all had at least some fracture steps. Polygonal relief patterns similar to those for 0 w/o Hf and partially fractured oxide particles were found in the surfaces of the underlying metal. Arc-melted 1 w/o Hf samples produced very similar results.

Laser clad 2 1/2 w/o Hf alloy produced a scale that remained intact after cooling from 1200°C. The scale was composed of an alumina matrix punctuated with hafnia-rich polycrystallites (Figure 8). The hafnia-rich particles appear to have a mean free distance of ~ 5 to 10 μm, which corresponds well to the dendrite spacing in the as-clad alloy. The only defects visible on the surface of the sample were some short intergranular cracks, often in the proximity of the hafnia particles. Cross-sectioning of this sample as shown in Figure 9 revealed an alumina scale with hafnia dispersoids (left of center) approximately 2 to 5 μm thick in intimate contact with the underlying metal along an irregular interface. Measurements of the number density and median length of hafnia dispersoids are given in Table VI. The number and size of these particles in the scale are similar to those values for Hf particles in the as-cast alloy as shown by comparing Table VI with Table IV. Some fractures reach the scale-metal interface, but most are contained within the scale (center of Figure 9). Hafnia particles beyond the main scale layer are encapsulated with alumina and may have been attached to the scale via an appendage at a high angle to the plane of polish.

In the case of the 2 1/2 w/o Hf alloy, arc-melting produced a less intact scale. On the left side of Figure 10, a scale consisting of hafnia dispersed in alumina that is similar to that seen for laser clad 2 1/2 w/o Hf is visible. The dendritic pattern of the as-cast alloy is clearly replicated in the scale. Some coating failures occurred on the right side of Figure 10 that contain both intergranular and transgranular fracture areas as evidenced by the presence of fracture steps and polygonal fracture surfaces. In cross-section, these samples resemble

closely those of laser clad 2 1/2 w/o Hf (Figure 9) although more failures at the scale-metal interface are observed in the arc-melted samples.

Table VI Quantitative Analysis of Hafnia Particles in the Cross-section of 2 1/2 w/o Hf Alloy Isothermally Oxidized in Air for 20 Hours

Sample	Particles Examined	10^6 Particles per mm^3	Median Length (μm)
Arc-melted	567	5.55	1.06
Laser clad	1240	14.0	0.75

Laser clad 2 1/2 w/o Hf alloy produced a scale under cyclic conditions which largely resembles the isothermal scale. Figure 11(a) indicates that a uniform scale remains except in a few small areas. Note that the scale is continuous over the areas corresponding to the dendrites and the interdendritic areas without any discontinuties due to the sigma phase. This scale is virtually identical to those grown isothermally at 1200 °C (Figure 8). Intergranular and transgranular fracture of both the hafnia and alumina takes place within the scale as shown in Figure 11(b). A small crack is visible in the alumina matrix (dark) in the center of Figure 11(b); this crack does not appear to penetrate to the scale-metal interface.

D.   Stresses due to Thermal Cycling

The first step in understanding the effects of thermal cycling upon the mechanical integrity of the system of an oxide film and a metal substrate was to develop a simple physical model of the process. In this model, the scale is of uniform thickness, t_s, and is in complete contact with the underlying metal of thickness, t_m, at the exposure temperature, T_i. No stresses are assumed to be present in either the film or the substrate prior to cooling. The scale grows on both sides of the metal substrate. For the samples tested, 1 μm < t_s< 10 μm and 0.5 mm < t_m< 1.0 mm. During the cooling of the sample, thermal gradients created within the scale and the metal are potential sources of residual stress because of thermal contraction in each of

these parts. If the linear thermal expansion coefficients of the scale and the metal are unequal, additional stresses will be developed. Those effects were considered independently.

The effect of the cooling rate was first considered. For the sake of this analysis, the maximum rate possible (1.7°C/sec) was used, and values of the properties were those for alumina to maximize the effect. Completely elastic behavior will be assumed. For an infinite plate of thickness x, [19]

$$\sigma = \frac{E\alpha_t x^2 \phi}{12(1-v)\alpha_d} \tag{1}$$

where
σ	=	Thermal stress arising from the cooling rate	
E	=	Young's modulus (340 GPa) [20]	
α_t	=	Linear coefficient of thermal expansion (LCTE) (8.7 x 10^{-6} °C^{-1}) [21]	
x	=	Thickness of plate (0.1 cm)	
ϕ	=	Cooling rate (1.7 °C/s)	
v	=	Poisson's ratio (0.35) [20]	
α_d	=	Thermal diffusivity (0.015 cm^2/s) [22]	

Substitution into (1) yields a stress of 0.43 MPa which is of no consequence compared to a compressive strength of 500 to 3000 MPa over the temperature range of 0 °C to 1200 °C. The sample can then be considered as an isothermal body.

The stress in the coating was then estimated using a thermoelastic analysis.[15,23] Assumptions include complete contact between the scale and the metal, no work hardening in the metal, no edge effects and a scale that is much thinner than the underlying metal. The stress in the scale is estimated by:

$$\sigma_s = E_s(\alpha_m - \alpha_s)(T - T_i) \tag{2}$$

where
σ	=	Stress in the scale
E_s	=	Young's modulus of the scale (340 GPa) [20]
α_s	=	LCTE of scale (8.7 x 10^{-6} °C^{-1}) [21]
α_m	=	LCTE of metal (18.0 x 10^{-6} °C^{-1}) [24]
T_i, T	=	Initial and final temperature, respectively

(Values in parentheses are mean values of the quantity over the interval of 20 to 1200 °C)

Since $T < T_i$, σ_s is negative so that the scale is in a compressive state of stress during the cooling process. Temperature variant values of these quantities were used to produce the plots of σ_s versus T for various T_i shown in Figure 12. Also shown in this plot are values of the compressive strength for monolithic low porosity alumina.[20] For $T_i = 1200$ °C, σ_s exceeds the strength of the alumina when $T \approx 850$ °C. Similar results were obtained earlier by Kumar et al.[15] Note that the stress/strength ratio continues to increase with further cooling. For a brittle coating material such as α-alumina, catastrophic failures would be expected.

4. Discussion

The effect of cooling to ambient after exposure upon the scale was predicted to be severe and is clearly demonstrated. Figure 12 shows that the stress induced in the scale is very large relative to the strength of the alumina. As noted earlier, data for monolithic ceramic components should be used with caution,[15] but it is clear that the mismatch in LCTE between the alloy and the alumina scale is sufficient to cause failure of the scale. The fact that the scale did not spall on 0 w/o Hf alloy after isothermal or cyclic exposure at 1000 °C for 20 hours but did after 60 minutes at 1200 °C, conditions that produce similar weight gains, indicates that the stresses due to the difference between the exposure and ambient temperatures is the dominating factor in the retention of scales without hafnia.

Response to this stress is a function of Hf content and the interaction between the Hf content and the processing method. The addition of Hf in amounts of ≈ 2 1/2 w/o dramatically reduces the rate of spallation as indicated in Figure 4. At 2 1/2 w/o Hf, and only at that level, laser cladding produces an additional improvement: the rate of spallation is below the limit of detection through 28 cycles. 0 w/o Hf alloy retains none of its scale, and 1 w/o Hf alloy retains mostly hafnia while 2 1/2 w/o Hf alloy retains nearly complete alumina-based scales, especially if laser clad. Any explanation of the oxidation behavior must account for the dependency of the resistance of thermal stress upon Hf content and processing method.

The failure mode of the scale is dependent upon the Hf content. Without Hf, the scale fractured intergranularly into large flakes. Crack propagation was perpendicular to the plane of the sample as shown in Figure 6. Addition of 1 w/o Hf produces very small spalled alumina particles and hafnia particles left embedded in the metal. The smooth facets and fracture steps on the hafnia particles indicate some transgranular fracture took place, (Figure 7). Addition of 2 1/2 w/o Hf increased the amount of transgranular fracture as shown in Figure 8. Fracture steps within both the hafnia and alumina in Figure 11(b) clearly represent transgranular fracture. Slip within α-alumina in the temperature range of interest is limited to 2 independent slip systems of the type $\{0001\}<11\bar{2}0>$ so that cross-slip is difficult.[25] Plastic deformation will be highly localized and will be accommodated by cleavage cracking. Coble and Parikh note that the proportion of transgranular fracture within alumina decreases with increasing temperature until at above about 1000 °C, the fractures are entirely intergranular.[26] These results suggest that the temperature at which the fractures occur decreases with increasing Hf content. Lower failure temperatures during thermal cycling means that a higher stress was resisted prior to failure.

Understanding how these features affect the performance of the scale can be achieved by applying the Griffith criterion to the triaxial state of stress induced in a monolithic elastic component quenched through a temperature difference, ΔT.[27] Combining these concepts indicates that the the fracture resistance of the material is dependent upon the length of existing cracks and ΔT. For $\Delta T < \Delta T_c$, a critical value, no fracture occurs due to crack propagation which translates into complete retention of strength. At $\Delta T = \Delta T_c$, the stress is sufficient to propagate cracks at very high speed and the strength drops sharply. Depending upon the size of the sample, this propagation could produce a catastrophic failure. If not, the crack reaches an equilibrium length so that further increases in ΔT do not produce any changes in the strength or crack length until $\Delta T_c'$ ($> \Delta T_c$) is reached where quasistatic or stable crack propagation

takes place and strength is steadily lost as ΔT is further increased. Monolithic polycrystalline alumina exhibits this behavior.[27,28]

Consideration of this model of thermal shock resistance explains the significance of the microstructural features in Figure 11(b). The fracture steps, whatever their origin, increase the toughness of the scale[25,26,29] so that a higher stress due to constrained cooling is needed to propagate cracks. The fact that increasing the hafnia content of the scale improves its retention indicates that the hafnia improves resistance to crack propagation in the scale by some means.

The most straightforward explanation is that the hafnia particles alters the mechanical properties of the scale according to the law of mixtures. Decreasing E while maintaining the yield strength would lessen the effects of thermal shock as suggested by equation (2). For hafnia, E is equal to 200 - 240 GPa for the temperature range of 0 °C to 1200 °C [30]. No data could be found for the strength of hafnia, but the strength of monoclinic zirconia, which is completely soluble in hafnia, has a compressive strength comparable to that for alumina[20]. Given that the scales contain less than 5 w/o hafnia, large changes in strength or E of the composite scale are unlikely. On the other hand, the hafnia does not appear to be a weaker phase that could relieve stress by promoting grain boundary sliding.

Transformation toughening does not explain the current results. When hafnia or zirconia transforms from tetragonal to monoclinic via a martensitic reaction ahead of an advancing crack tip, the stress ahead of the tip is lowered and the tip is blunted, a phenomenon known as crack shielding[31,32]. However, the M_s temperature for hafnia is estimated at 1620 °C [33]. Therefore, the martensitic reaction is not likely to occur in hafnia in the samples tested here.

Another crack shielding mechanism is more credible. Microcracking in an oxide matrix can occur by the cooling of an oxide phase having anisotropy in thermal contraction[28,31,32]. These microcracks reduce the effective Young's modulus and produce a permanent strain which can impede the propagation of cracks. Ceramic composites containing m-zirconia, including those with alumina matrices, have been shown to experience toughening via this mechanism[28,33]. Garvie and Goss found that the strength of a composite of alumina and m-zirconia gradually decreased with increasing ΔT, which is indicative of quasi-static crack growth[28]. The ability of hafnia to promote microcrack toughening can be predicted from this work. Both monoclinic zirconia and hafnia exhibit dramatic anisotropy in thermal expansion: the LCTE along c is 1.5 to 2 times that along a in the temperature range of 0-1100°C so that their potential for microcracking is established[21]. Hafnia monoliths display such microcracking[30]. Figure 11(b) (center) displays small (< 10 µm) cracks stopping within the alumina matrix while in the proximity of hafnia-rich polycrystallites. While this evidence is not absolutely conclusive, the potential for the microcrack toughening mechanism exists and at least some physical verification has been made of its action.

The effects of laser cladding can now be explained. Laser cladding produced about 3 times as many Hf-rich particles in the 2 1/2 w/o Hf alloy as did arc-melting. This increase in Hf particles increases the number of hafnia particles in the resulting scale. The smaller dendrite spacing provided by laser cladding reduces the mean free distance between these particles as well. By providing more potential microcracking sites per unit volume, the efficiency of the toughening mechanism is enhanced[31]. A Griffith-type crack has a reduced chance to reach the critical length before encountering a microcracking site as a result of laser cladding the alloy.

Luthra and Briant have suggested that different mechanisms for scale retention via RE additions could occur depending upon the base alloy[13]. They found a residual compressive strain of about 1 % in alumina scales retained on FeCrAlY but almost none in the scales left on NiCoCrAlY and NiCrAlY alloys. In all cases, Y additions promoted the retention of the scale

during cooling. Those authors did not find any significant correlation between sulfur segregation and scale retention but concluded that thermal strains in the scale were somehow relieved without spallation and that none of the mechanisms listed in the Introduction could produce that relief. They suggested that yttrium might cause microcracking but did not describe the origin of microcracks in alumina scales.

Based upon the results of this study, a new mechanism is proposed. Large compressive stresses are produced during cooling in alumina scales formed on NiAlCr because of constraint by the underlying metal which can be sufficient to cause primarily intergranular failure of the alumina scale (if the exposure temperature is high enough) which results in spallation of the scale. Sufficient levels of Hf in the alloy produce hafnia dispersoids in the resulting scale which increase the scale toughness as evidenced by its resistance to any failure and the increased tendency to undergo transgranular fracture when failures do occur. The increased toughness of the scale may be due to microcracking caused by the anisotropic thermal contraction of monoclinic hafnia. Laser cladding enhances this process by providing a greater number density of hafnium-rich particles that are the precursors of the hafnia polycrystallites in the scale so that more possible sites of microcracking are produced.

Other mechanisms proposed in the literature may be considered and rejected as possible means of explaining the beneficial effect of Hf in this study. The graded seal mechanism is rejected because the aggregate LCTE of m-hafnia is lower than that for alumina and Figure 10 shows that the hafnia is dispersed within the alumina instead of forming a layer between the alumina and the alloy. Sulfur gettering is counterindicated because laser clad 2 1/2 w/o Hf alloy outperformed all three arc-melted alloys despite having 3 times as much sulfur. The action of Hf as a vacancy sink is not supported because very few voids of sufficient size to affect adherence were found at or near the scale-metal interface of any of the samples. Mechanical pegging is unlikely despite the formation of oxide appendages because these "pegs" would served to further constrain the scale during cooling.

Conclusions

A new mechanism has been proposed to explain the beneficial effect of Hf additions to NiAlCr alloys upon alumina scale retention. Spallation of alumina scales on a NiAlCr alloy during cooling was found to result from the action of compressive stresses generated by constraint by the underlying metal. Additions of ≈ 2 1/2 wt % Hf to the alloy produce a alumina-rich scale containing a dispersion of hafnia polycrystallites which is associated with improved scale toughness. The improvement in toughness may result from microcracking initiated by the anisotropic thermal contraction of these polycrystallites. Laser cladding the 2 1/2 w/o Hf alloy provides a greater number density of Hf-rich particles and a smaller dendrite spacing separating the particles which are the precursors of the hafnia polycrystallites in the scale. By increasing the number density of the polycrystallites in the scale, microcrack toughening is enhanced so that scale retention is improved.

Acknowledgments

References

1. C. Ribaudo, S. Sircar, and J. Mazumder: *Metall. Trans. A.*, 1989, vol. 20A, p. 2489.

2. P. A. Kofstad, A. Rahmel, R. A. Rapp, and D. L. Douglass: *Oxid. Met.*, 1989, vol. 32, p. 125.

3. D. P. Whittle, and J. Stringer: *Phil. Trans. R. Soc.*, 1980, vol. A295, p. 309.

4. I. M. Allam, D. P. Whittle, and J. Stringer: *Corrosion and Erosion of Metals*, ed. K. Natesan, TMS-AIME, Warrendale, PA, 1980, p. 103.

5. J. K. Tien, and F. S. Pettit: *Metall. Trans.*, 1972, vol. 3, p. 1587.

6. J. G. Smeggil, A. W. Funkenbusch, and N. S. Bornstein: *Metall. Trans. A*, 1986, vol. 17A, p. 923.

7. J. L. Smialek,: *N. L. Peterson Memorial Symposium: Oxidation of Metals and Associated Mass Transport*, ed. M. A. Dayananda, S. J. Rothman, and W. E. King, TMS-AIME, Warrendale, PA., 1987, p. 297.

8. D. R. Sigler: *Oxid. Met.*, 1988, vol. 29, p. 23.

9. D. R. Sigler: *Oxid. Met.*, 1989, vol. 32, p. 337.

10. J. C. Smialek: *Metall. Trans. A*, 1991, vol. 22A, p. 739.

11. H. Pfeiffer: *Werkstoffe Korros.*, 1957, vol. 8, p. 594.

12. F. A. Golightly, F. H. Stott, and G. C. Wood: *Oxid. Met.*, 1976, vol. 10, p. 163.

13. K. L. Luthra, and C. L. Briant: *Oxid. Met.*, 1986, vol. 26, p. 397.

14. S. Sircar, C. Ribaudo, and J. Mazumder: *Metall. Trans. A*, 1989, vol. 20A, p. 2267.

15. A. Kumar, M. Nasrallah, and D. L. Douglass: *Oxid. Met.*, 1974, vol. 8, p. 227.

16. C. S. Giggins, and F. S. Pettit: *J. Electrochem. Soc.*, 1971, vol. 118, p. 1782.

17. E. E. Underwood: *Quantitative Stereology*, Addison-Wesley, Reading, MA, 1970, p. 109.

18. B. Pieraggi: *Oxid. Met.*, 1987, vol. 27, p. 177.

19. W. D. Kingery, H. K. Bowen, and D. R. Uhlmann: *Introduction to Ceramics*, 2nd ed., John Wiley and Sons, New York, 1976, p. 819.

20. G. V. Samsonov: *The Oxide Handbook*, IFI/Plenum, New York, 1973, p. 225, 233.

21. Y. S. Touloukian, R. K. Kirby, R. E. Taylor, and T. Y. R. Lee: *Thermalphysical Properties of Matter: Thermal Expansion of Non-Metallic Solids*, vol. 13, 1977, IFI/Plenum, New York, p. 252, 451.

22. Y. S. Touloukian, R. W. Powell, C. Y. Ho, and M. C. Nicoleau: *Thermalphysical Properties of Matter: Thermal Diffusivity*, vol. 10, IFI/Plenum, New York, 1973, p. 378.

23. C. H. Hsueh, and A. G. Evans: *Ceramic Containing Systems: Mechanical Aspects of Interfaces and Systems*, ed. A. G. Evans, Noyes Publications, Park Ridge, NJ, 1986, p. 176.

24. Y. S. Touloukian, R. K. Kirby, R. E. Taylor, and P. D. Desai: *Thermalphysical Properties of Matter: Thermal Expansion of Metallic Elements and Alloys*, vol. 12, 1975, IFI/Plenum, p. 1216.

25. R. J. Stokes: *Fracture: An Advanced Treatise*, ed. H. Leibowitz, Academic Press, New York, 1972, p. 157.

26. R. L. Coble, and N. M. Parikh: *Fracture: An Advanced Treatise*, ed. H. Leibowitz, Academic Press, New York, 1972, p. 245.

27. D. P. H. Hasselman: *J. Am. Ceram. Soc.*, 1969, vol. 52, p. 600.

28. R. C. Garvie, and M. F. Goss: *Advanced Ceramics II*, ed. S. Somiya, Elsevier Applied Science, New York, 1988, p. 69.

29. F. J. P. Clarke, H. G. Tattersall, and G. Tappin: *Proc. Brit. Cer. Soc.*, vol. 6, 1966, p. 163.

30. S. L. Dole, O. Hunter, F. W. Calderwood, and D. J. Bray: *J. Am. Ceram. Soc.*, 1978, vol. 61, p. 486.

31. A. G. Evans: *Science and Technology of Zirconia II*, ed. N. Claussen, M. Rühle, and A. Heuer, Am. Ceram. Soc., Columbus, OH, 1984, p. 193.

32. M. V. Swain: *Advanced Ceramics II*, ed. S. Somiya, Elsevier Applied Science, New York, 1988, p. 45.

33. I-Wei. Chen, and V-H. Chiao: *Science and Technology of Zirconia II*, ed. N. Claussen, M. Rühle, and A. Heuer, Am. Ceramic Soc., Columbus, OH, 1984, p. 33.

LIST OF FIGURES

Figure 9.   Cross-section of sample of laser clad 2 1/2 w/o Hf after oxidation at 1200 °C for 20 hours in air (same sample as in Figure 8). The scale runs vertically and left of center of the micrograph. The underlying metal is to the right of the scale (SEM micrograph).

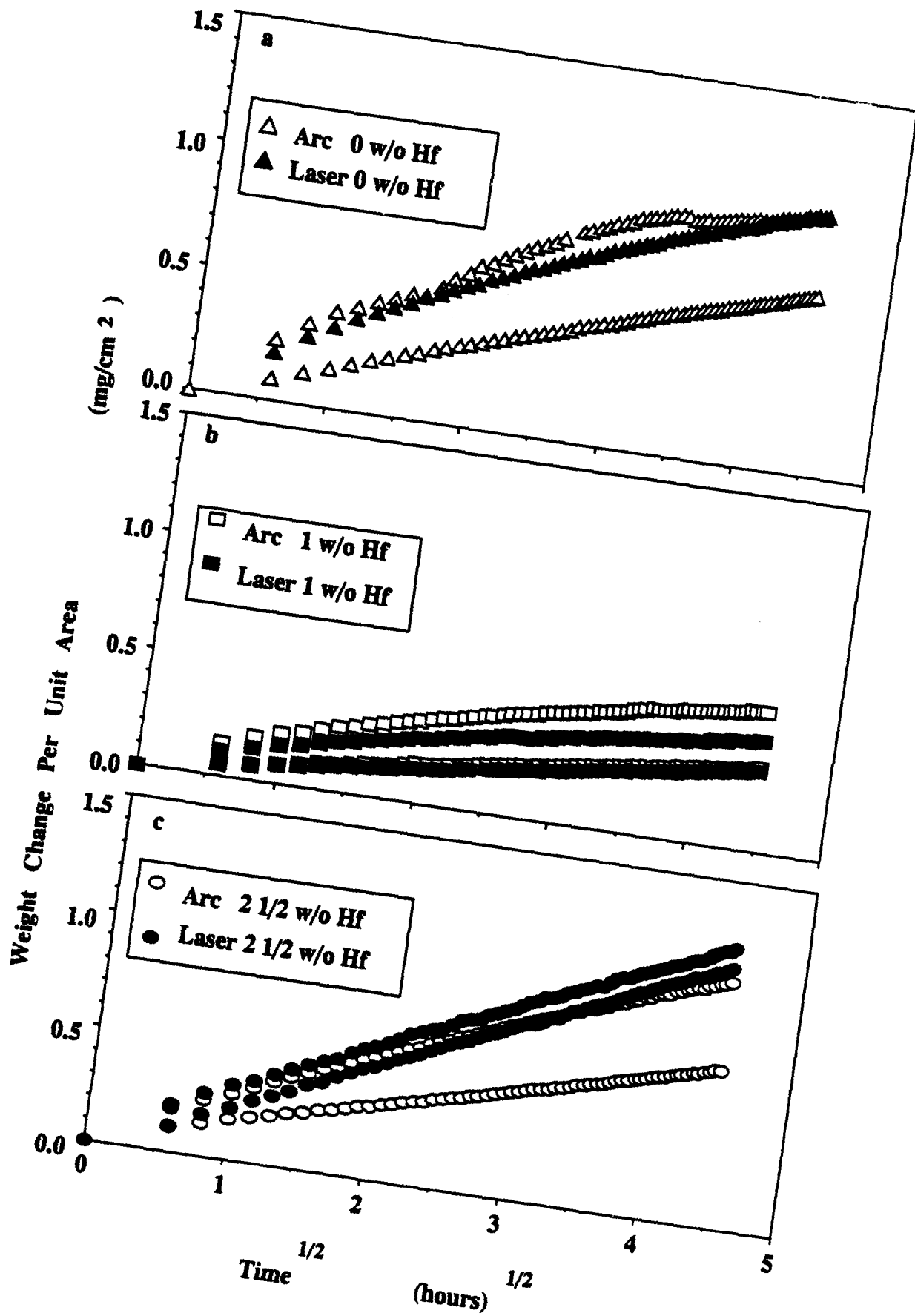Figure 10.   Surface of arc-melted 2 1/2 w/o Hf alloy after oxidation at 1200 °C for 20 hours in air. Spall areas are visible at the upper right hand quadrant (SEM micrograph).
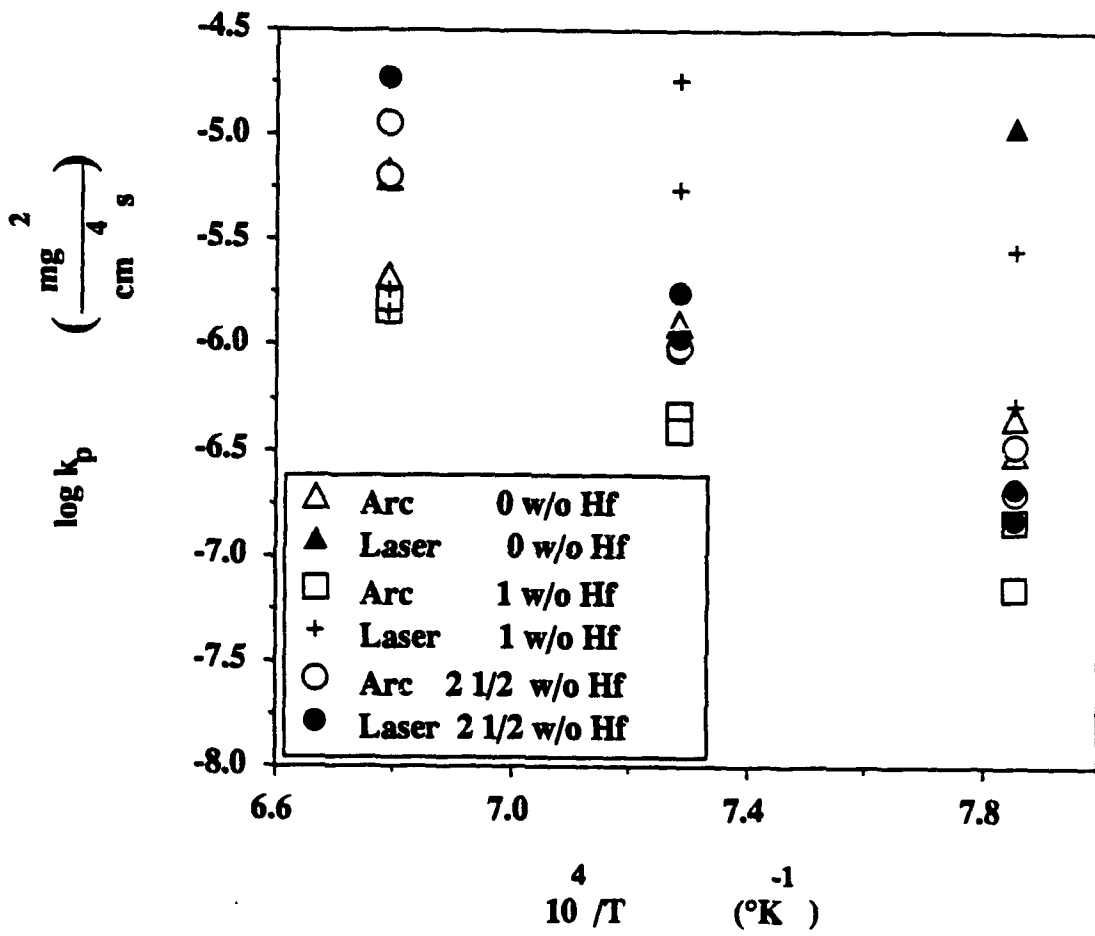
Figure 11.   Surface of retained scale on laser clad 2 1/2 w/o Hf after 20 cycles at 1200 °C in air: (a) overview and (b) a detail of the failure area in the center of (a) (SEM micrograph).
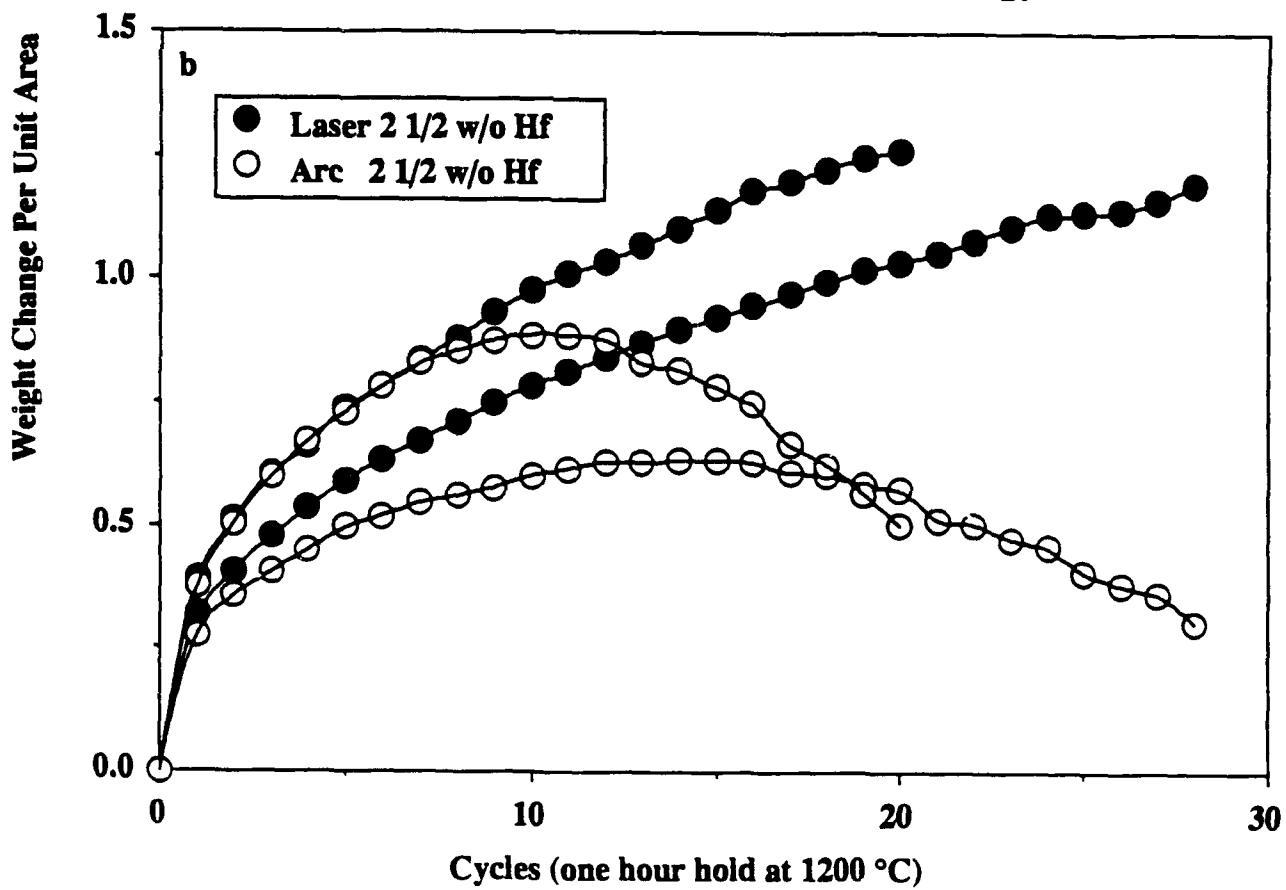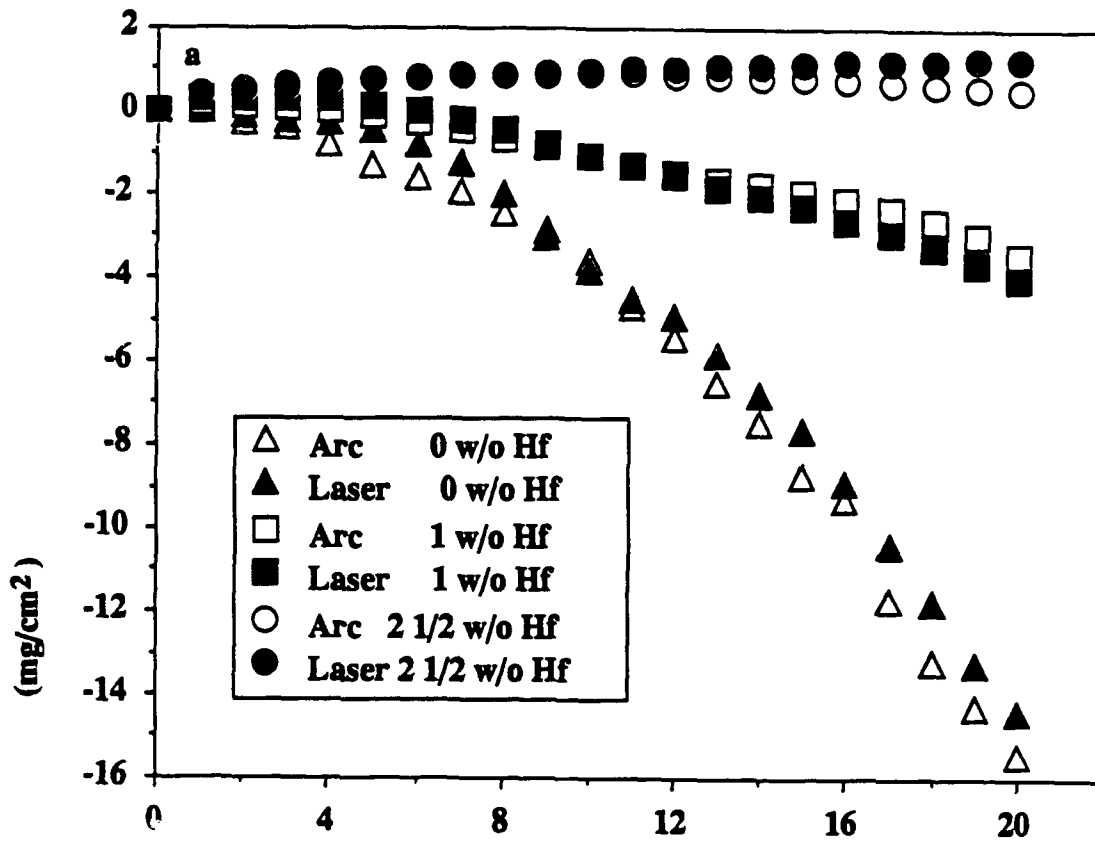
Figure 12   Estimated compressive stress in the alumina scale as a function of temperature. Plots are shown for initial temperatures of 800, 1000 and 1200 °C. A plot of the compressive strength of low porosity alumina is also given for comparison.[20]
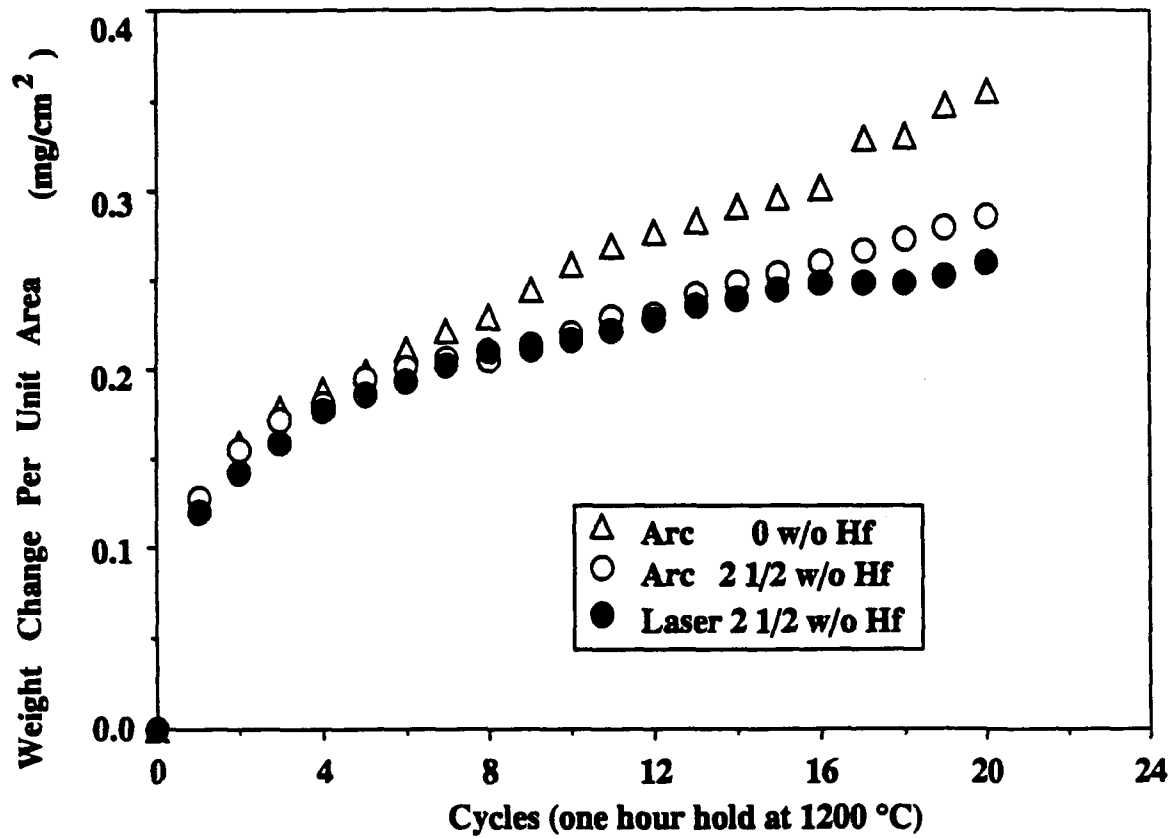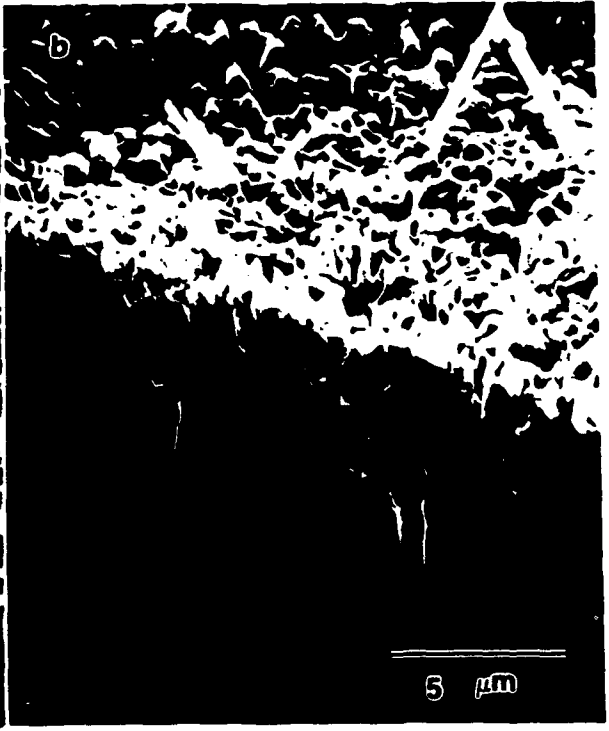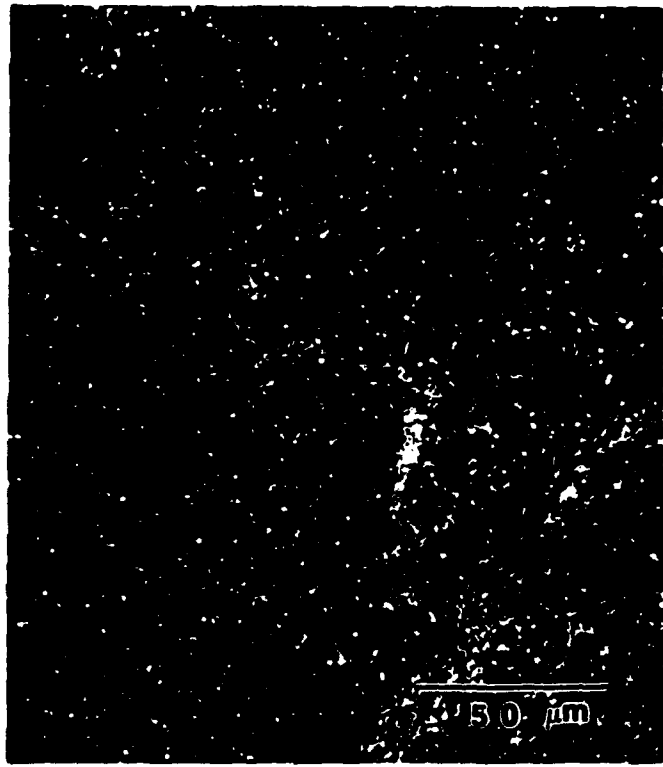
Figure axes (reading from the chart):

- Panel a: y-axis (mg/cm^2), data series — Arc 0 w/o Hf (△), Laser 0 w/o Hf (▲)
- Panel b: y-axis label **Weight Change Per Unit Area**, data series — Arc 1 w/o Hf (□), Laser 1 w/o Hf (■)
- Panel c: data series — Arc 2 1/2 w/o Hf (○), Laser 2 1/2 w/o Hf (●)
- x-axis: Time$^{1/2}$ (hours)$^{1/2}$, ranging 1 to 5

1.0 μm

10 μm

500 µm